

High-resolution observations at 3.6 cm of seventeen FR II radio galaxies with $0.15 < z < 0.30$

M. J. Hardcastle,^{*} P. Alexander, G. G. Pooley and J. M. Riley

Mullard Radio Astronomy Observatory, Cavendish Laboratory, Madingley Road, Cambridge CB3 0HE

Accepted 1997 January 29. Received 1997 January 29; in original form 1996 September 11

ABSTRACT

We present high-resolution VLA observations at 8.4 GHz of the seventeen FR II radio galaxies with $0.15 < z < 0.30$ and $\theta_{\text{LAS}} < 190$ arcsec from the sample of Laing, Riley & Longair, together with 5-GHz MERLIN observations of one source. Jets have been discovered in 3C 20, 4C 14.11, 3C 234 and 3C 436, and well imaged for the first time in a number of other objects; the fraction of objects in the sample with definite or probable jets is 76 per cent. The properties of the hotspots of the objects and their implications for models of radio sources are discussed.

Key words: galaxies: active – galaxies: jets – radio continuum: galaxies.

1 INTRODUCTION

In earlier papers (Black et al. 1992, hereafter B92; Leahy et al. 1997, hereafter L97), observations are presented of part of a sample of 29 radio galaxies taken from the 3CR catalogue (Spinrad et al. 1985) with $z < 0.15$ and 178-MHz radio power (P_{178}) greater than $1.5 \times 10^{25} \text{ W Hz}^{-1} \text{ sr}^{-1}$. The primary aim of these observations was to provide high-resolution images of the hotspots in these objects. Hotspots are the termination points of the relativistic beams believed to emanate from the nuclei of extragalactic radio sources. Much theoretical and numerical work has been undertaken in an attempt to understand the physics of these regions, but this has been hampered by the lack of sufficiently detailed images for a large number of objects. B92 aimed to fill this observational gap. Their detailed images, however, raised a number of new questions, since the structures revealed were complex and disparate. Earlier observations (e.g. Perley 1989; Laing 1989, hereafter L89) had suggested that hotspots tended to have no more than two components, but several objects in the $z < 0.15$ sample had more complicated structures which could not be classified as having at most one ‘primary’ (most compact) and one ‘secondary’ (more diffuse) component (using the classification of L89). L97 were able to identify some trends in the hotspot structures of the sample, and in many cases to define a primary component which could plausibly be identified as the current termination of the jet. It is not clear to what extent these observations are in conflict with the results of L89, which were based on observations of objects with $z > 0.3$; it is possible that the different hotspot structures in the $z < 0.15$ sample were a result of the proximity of these objects in radio power to the boundary ($P_{178} \approx 2 \times 10^{25} \text{ W Hz}^{-1} \text{ sr}^{-1}$) between FRI and FR II structures (Fanaroff & Riley 1974; hereafter FR).

These observations also revealed a number of new jets. Past observations of FR II radio galaxies had failed to detect jets in

significant numbers; in a review of the observations, Muxlow & Garrington (1991) suggested that no more than 10 per cent of FR II radio galaxies had detected jets, although jets are much more plentiful in FR II quasars of similar power. In contrast, the observations described in B92 and L97 show jets to be present in 50 to 70 per cent of their low-redshift sample (Black 1992, 1993; L97). Jets are believed to be the tracers of the beams carrying relativistic particles to the hotspots [throughout this paper, following Hughes & Miller (1991), we will retain this distinction between the beam, the stream of relativistic particles, and the jet, its visible manifestation]. Observations of statistically significant numbers of jets should provide us with information both on the power carried by the beam, which can be related to other indicators of the output of the active galactic nucleus (AGN), and on the factors that affect its efficiency. Again, though, it is unclear whether this high jet detection rate is a consequence of the low luminosity of the $z < 0.15$ objects, or whether the observations of B92 and L97 were simply superior to and more systematic than those that had preceded them.

To address both these questions we have chosen a new sample of objects, which when combined with the sample of B92 extends it to higher radio power and redshift. In this paper we will discuss the selection of this new sample and the images that we have obtained, with particular reference to the jet and hotspot physics of the individual sources, and summarize the jet and hotspot properties of this sample. In later papers we will discuss the physics of the jets and hotspots in the combined sample of objects with $z < 0.3$.

Throughout this paper we take $H_0 = 50 \text{ km s}^{-1} \text{ Mpc}^{-1}$ and $q_0 = 0$. Spectral index α is defined in the sense $S \propto \nu^{-\alpha}$. B1950 coordinates are used. Position angles are defined east of north.

2 SAMPLE SELECTION

To extend the sample of B92 to larger redshifts and higher luminosities, we selected the 21 FR II radio galaxies in the

^{*} Present address: H. H. Wills Physics Laboratory, University of Bristol, Royal Fort, Tyndall Avenue, Bristol BS8 1TL.

Table 1. The sample of radio sources.

Source	IAU name	z	S_{178} (Jy)	α	P_{178} (10^{24} W Hz $^{-1}$ sr $^{-1}$)	scale (kpc/arcsec)	LAS (arcsec)	Size (kpc)	RM (rad m $^{-2}$)
4C 12.03	0007+124	0.156	10.9	0.87	104	3.66	215.0	787	−4
3C 20	0040+517	0.174	46.8	0.66	543	3.99	53.6	214	159
3C 33.1	0106+729	0.181	14.2	0.62	178	4.12	227.0	935	−15
3C 61.1	0210+860	0.188	34.0	0.77	462	4.21	186.0	782	−
3C 79	0307+169	0.2559	33.2	0.92	930	5.33	89.0	474	−19
4C 14.11	0411+141	0.206	12.1	0.84	208	4.55	116.0	527	−19
3C 123	0433+295	0.2177	206.0	0.70	3873	4.74	37.8	179	−324
3C 132	0453+227	0.214	14.9	0.68	269	4.68	22.4	105	−38
3C 153	0605+480	0.2771	16.7	0.66	524	5.63	9.1	51	34
3C 171	0651+542	0.2384	21.3	0.87	505	5.06	32.5	165	43
3C 173.1	0702+749	0.292	16.8	0.88	624	5.83	60.5	353	−29
3C 219	0917+458	0.1744	44.9	0.81	536	4.00	190.0	760	−19
3C 234	0958+290	0.1848	34.2	0.86	466	4.18	112.0	469	42
3C 284	1308+277	0.2394	12.3	0.95	299	5.08	178.1	904	−4
3C 300	1420+198	0.272	19.5	0.78	604	5.56	100.9	561	−6
3C 319	1522+546	0.192	16.7	0.90	249	4.31	105.2	453	7
3C 349	1658+471	0.205	14.5	0.74	242	4.53	85.9	389	12
3C 381	1832+474	0.1605	18.1	0.81	181	3.75	73.2	274	25
3C 401	1939+605	0.201	22.8	0.71	362	4.46	23.6	105	−
3C 436	2141+279	0.2145	19.4	0.86	365	4.69	109.1	511	−53
3C 438	2153+377	0.290	48.7	0.88	1783	5.81	22.6	131	−

Column 4 lists the 178-MHz flux of the source. Column 5 gives the low-frequency (178–750 MHz) spectral index. Column 6 lists the luminosity at 178 MHz. Largest angular size, in column 8, was measured from the best available VLA maps. Integrated rotation measure, in column 10, is taken from Simard-Normandin, Kronberg & Button (1981), where available. All other data points are taken from LRL, with the 178-MHz flux corrected to the scale of Baars et al. (1977).

sample of Laing, Riley & Longair (1983, hereafter LRL) with $0.15 < z < 0.3$: see Table 1. The sources that met the redshift criteria but which were classed as FR Is by LRL were 3C 28 (Feretti et al. 1984), 3C 288 (Bridle et al. 1989) and 3C 346 (Spencer et al. 1991). A decision was taken at an early stage not to observe the four largest sources in the sample, 4C 12.03, 3C 33.1, 3C 61.1 and 3C 219, both for economy in observing time and because these sources were already relatively well-studied (Leahy & Perley 1991, hereafter LP; Rudnick 1984; Clarke et al. 1992). The remaining sources were observed with the VLA.

3 OBSERVATIONS AND DATA REDUCTION

We adopted an observing strategy similar to that described by B92. The 8-GHz receivers of the VLA were used, both for consistency with the results of B92 and because their high sensitivity makes them ideal for observations of this type. We observed each source using VLA configurations chosen both to sample the uv plane adequately on the shortest baselines necessary and to provide good resolution when mapping the detailed source structure. For a typical large source in the sample we observed for 10 min at D array, 45 min at C array, 1 h at B array and 1.5 h at A array. We did not observe the smaller sources (largest angular size, LAS, less than 60 arcsec) in the D configuration, and the very smallest sources (LAS less than 20 arcsec) were only observed with B and A arrays. Sources smaller than 30 arcsec were only observed for half an hour in B array and an hour in A array. The largest sources were observed for two hours at A array. Because some of our data were provided by other workers, and for other reasons beyond our control, actual times on source varied from this plan in some cases. The complete observational information for the sample is given in Table 2. The typical full resolution (FWHM of the restoring Gaussian) of the resulting

images is 0.23 arcsec, corresponding at these distances to a linear resolution of approximately 1 kpc. The typical off-source noise on the maps is 30 μ Jy.

Except where otherwise specified, the two standard 8-GHz observing frequencies of 8.415 and 8.465 GHz were used. We required that bandwidth smearing should affect peak fluxes by less than 5 per cent. Because of the angular size restriction on the sources that we observed, a bandwidth of 50 MHz (the largest bandwidth of the VLA) met this requirement for all observations at B, C and D arrays. At A array we observed sources with sizes less than 45 arcsec with 50-MHz bandwidth, sources with sizes less than 90 arcsec with 25-MHz bandwidth, and the remainder with 12.5-MHz bandwidth.

As is usual at the VLA, 3C 48 and 3C 286 were used as primary flux calibrators, and 3C 286 and 3C 138 as polarization position angle calibrators. Secondary phase calibrators were observed at intervals of approximately half an hour (sometimes less). Typically one or more of these secondary calibrators was observed at a number of parallactic angles and used for polarization calibration. In the large VLA configurations, observations of a given source were usually split in LST and interleaved with other observations to improve coverage of the uv plane.

The data were reduced with the NRAO AIPS software. Observations at each VLA configuration of a particular source were initially treated separately; each data set was imaged and phase self-calibrated several times, and data editing was done at this stage. (Amplitude self-calibration was rarely necessary.) The data sets from the different configurations were then merged with no reweighting. Positional alignment was ensured by self-calibrating one data set with images from another. The combined data sets were used to produce images at different resolutions by suitable weighting of the uv plane; at this stage the data sets at the two observing

Table 2. Observational information for the FR II sample observed with the VLA.

Source	A configuration		B configuration		C-configuration		D-configuration	
	Date of observation	t_{int} (mins)	Date of observation	t_{int} (mins)	Date of observation	t_{int} (mins)	Date of observation	t_{int} (mins)
4C 12.03	Not observed	—	Not observed	—	Not observed	—	Not observed	—
3C 20	1988/11/25 ^a	600	1994/06/23	60	1989/09/01 ^b	80	Not observed	—
3C 33.1	Not observed	—	Not observed	—	Not observed	—	Not observed	—
3C 61.1	Not observed	—	Not observed	—	Not observed	—	Not observed	—
3C 79	1995/08/06	90	1994/06/23	60	1989/09/01 ^b	120	1989/12/14 ^b	15
4C 14.11	1995/08/06	150	1994/06/23	60	1993/08/03	40	1993/11/27	15
3C 123	1995/08/06	60	1994/06/23	60	1993/08/03	40	Not observed	—
3C 132	1995/08/06	60	1994/06/23	30	Not observed	—	Not observed	—
3C 153	1995/08/06	60	1994/06/23	30	Not observed	—	Not observed	—
3C 171	1995/08/06 ^c	60	1992/01/11 ^d	35	1992/04/10 ^d	25	Not observed	—
3C 173.1	1995/08/06	90	1994/06/23	60	1993/08/03	40	1993/11/27	15
3C 219	Not observed	—	Not observed	—	Not observed	—	Not observed	—
3C 234	1995/08/06	120	1994/06/23	60	1993/08/03	45	1995/11/27	15
3C 284	Not observed	—	1992/01/11 ^d	30	1992/04/10 ^d	30	1992/08/22 ^d	20
3C 300	1995/08/06 ^c	120	1992/01/11 ^d	30	1992/04/10 ^d	25	1993/08/26 ^d	10
3C 319	Not observed	—	1994/06/23	60	1993/08/03	50	1993/11/27	15
3C 349	1995/08/06	90	1994/06/23	60	1993/08/03	50	1993/11/27	15
3C 381	1995/08/06	90	1995/11/27	30	1993/08/03	50	1993/11/27	10
3C 401	1995/08/06	60	1994/06/23	30	1993/08/03	40	Not observed	—
3C 436	1995/07/23	120	1994/06/23	60	1993/08/03	50	1993/11/27	10
3C 438	1995/08/06	60	1994/06/23	30	1993/08/03	50	1993/11/27	10

^a Observations by W. Cotton and others from the VLA archives; observed at frequencies of 8.411 and 8.711 GHz.^b Data kindly supplied by J. P. Leahy.^c Observed at frequencies of 8.065 and 8.115 GHz.^d Data kindly supplied by K. M. Blundell; observed at 8.065 GHz only.

frequencies were treated as a single data set at an intermediate frequency. The AIPS task IMAGR was the main tool used, particularly at low resolutions, but when mapping complicated structure in total intensity we often used a combination of IMAGR and the maximum-entropy deconvolution task VTEST, as described in B92. The imaging method used for each total-intensity map presented is listed in Table 4 (later). Imaging of the Stokes parameters Q and U was always done with IMAGR.

4 SOURCES IN DETAIL

In Table 3 we list the 8-GHz total and core fluxes of each source, together with information on previous radio observations and spectral classifications. The objects are classed in Table 3 as narrow-line (NLRG), broad-line (BLRG) or low-excitation, following the definitions of Laing et al. (1994). For some objects we also discuss in the text optical or X-ray observations that provide clues to the sources' environments. Except where otherwise stated, the information on galaxy identifications, redshifts and magnitudes is taken from Laing & Riley's update of the information presented in LRL (in preparation).

Our own maps are presented at several resolutions for most sources, in an attempt to show both the large-scale structure and details of the hotspots and jets (where present). The resolution of low-resolution maps is generally chosen to give 50 beamwidths across the source; the resolution of the highest-resolution maps is the best that could be obtained from the data set for each source. The properties of the images shown are summarized in Table 4. Negative contours are dashed on all contour maps.

Polarization maps are also shown. On such maps the contours are deliberately widely spaced so as not to obscure the polarization vectors. Vectors are only plotted where both the total intensity and

the polarized intensity exceed three times the rms noise. The vector lengths represent the *degree* of polarization (corrected for Ricean bias) and the directions are perpendicular to the E -vector; they are therefore in the direction of the magnetic field if Faraday rotation is negligible. At 8.4 GHz, Faraday rotation is significant (involving corrections of $\geq 5^\circ$ to the position angles of the magnetic field vectors) if the rotation measure (RM) towards a given point of the source is greater than about 70 rad m^{-2} . However, the only information available for most objects in this sample is the integrated rotation measure, which constitutes an average (weighted by polarized flux density) over the source. While a high integrated RM implies that rotation measure is high over at least some part of the source, a low integrated RM does *not* necessarily imply the converse. In the text we therefore point out sources with high integrated RM, but it must be borne in mind that in general the magnetic field vectors we plot may deviate significantly from the true magnetic field direction even in sources with low integrated RM.¹

For some sources maps of spectral index between 1.4 and 8.4 GHz are discussed; to ensure that the effective beam sizes of both maps were the same, they were made by imaging the uv data sets in total intensity with matched longest baselines, adjusting the weighting of the two truncated data sets so that similarly sized Gaussians could be fitted to the inner regions of the dirty beam, cleaning to convergence and convolving with identical circular Gaussians larger than the largest axis of the fits to the beam. The 1.4-GHz data sets used for this were kindly supplied by J. P. Leahy from the observations described in LP.

¹ Leahy, Pooley & Riley (1986) show for several of our objects (3C 234, 3C 284, 3C 300 and 3C 319) that the variation in rotation measure on 5-arcsec scales across the source is too small to be significant for our observations. High-resolution RM maps are not in general available, however.

Table 3. 8-GHz radio data, optical classifications and previous observations for the objects discussed in Section 4.

Source	Freq. (GHz)	Total flux (Jy)	Core flux (mJy)	Error (mJy)	Optical class	Optical reference	Previous radio map reference
3C 20	8.44	2.29	3.32	0.06	N	1,2	9, 10, 11, 12, 13
3C 79	8.44	0.694	6.04	0.01	N	2	11, 14, 15, 16
4C 14.11	8.44	0.500	29.69	0.03	E	2	17
3C 123	8.44	9.44	108.9	0.3	E	2,3	11, 12, 18, 19
3C 132	8.44	0.674	4.1	0.2	E	4	20
3C 153	8.44	0.712	< 0.5		E	2	20, 21, 22
3C 171	8.06	0.690	2.0	0.1	N	4,5	23, 24, 25
3C 173.1	8.44	0.461	9.64	0.02	E	6	17, 26
3C 234	8.44	0.919	34.46	0.04	N/B?	7	20, 27, 28, 29, 30
3C 284	8.06	0.340	2.79	0.02	N	6	31
3C 300	8.06	0.645	6.2	0.1	N	6	15, 24, 31, 32
3C 319	8.44	0.362	< 0.3		E	6	31, 33, 34
3C 349	8.44	0.723	24.21	0.02	N	6	17
3C 381	8.44	0.906	4.7	0.1	B	8	17
3C 401	8.44	0.844	28.54	0.03	E	6	28
3C 436	8.44	0.592	17.90	0.02	N	6	35, 36
3C 438	8.44	0.780	16.2	0.1	E	6	9, 17

Column 2 lists the effective frequency of observation for each object. Column 3 gives the total flux at that frequency, measured by integration on suitable maps. (Because of slight undersampling, the fluxes given for 3C 132, 3C 171 and 3C 284 may be underestimates.) Column 4 lists the core flux, taken to be the integrated flux of a Gaussian fitted to the core with the AIPS task IMFIT except where no core was detected, and column 5 gives the error assigned by IMFIT. (The core fluxes of 4C 14.11 and 3C 79 are variable; see the text.) Column 6 gives the optical type as broad-line (B), narrow-line (N) or low-excitation (E) (3C 234's classification is uncertain: see the text). References used to make this classification are given in column 7. References to previous radio maps are given in column 8. References are 1: Lawrence et al. (1986); 2: Laing, private communication; 3: Spinrad (1978); 4: Laing et al. (1994); 5: Eracleous & Halpern (1994); 6: Rawlings et al. (1989); 7: Antonucci (1982); 8: Grandi & Osterbrock (1978); 9: Laing (1981); 10: Laing (1982); 11: Stephens (1987); 12: Meisenheimer et al. (1989); 13: Hiltner et al. (1994); 14: Spangler, Myers & Pogge (1984); 15: Burch (1979); 16: Myers & Spangler (1985); 17: Leahy & Perley (1991); 18: Riley & Pooley (1978); 19: Cox, Gull & Scheuer (1991); 20: Neff, Roberts, & Hutchings (1995); 21: Lonsdale & Morison (1983); 22: Akujor et al. 1991; 23: Heckman, van Breugel & Miley (1984); 24: Blundell (1994); 25: Blundell (1996); 26: Giovannini et al. (1988); 27: Dreher (1981); 28: Burns et al. (1984); 29: Alexander (1987); 30: Zukowski (1990); 31: Leahy & Williams (1984); 32: Alexander & Leahy (1987); 33: Bridle & Fomalont (1979); 34: Macklin (1983); 35: Riley & Pooley (1975); 36: Rawlings (1987).

Some definition of terms is necessary in order to describe sources in a consistent way. Components that are thought to be tracers of the beam before its impact at the working surface are classified as jets or, if they fail to meet the criteria of Bridle & Perley (1984), as possible jets. We follow L97 in describing as a hotspot any feature that is not part of a jet and which has a largest dimension smaller than 10 per cent of the main axis of the source, a peak brightness greater than 10 times the rms noise, and a separation from nearby peaks by a minimum falling to two-thirds or less of the brightness of the fainter peak. The most compact component is referred to as the primary hotspot, following L89, and the remaining components as the secondary hotspot or spots. We use this definition rather than the more restrictive one of Bridle et al. (1994) because our aim at this stage is to include as much as possible of the structure apparently associated with the beam termination in our discussion. For each source we will therefore try to identify the primary and secondary hotspots and to discuss possible models for the fluid flow.

4.1 3C 20

3C 20 is a well-studied object because of the prominent double hotspot in the E lobe. The western hotspot is an optical synchrotron source, and the eastern lobe is the more depolarized (Hiltner et al. 1994).

An unusually low fraction of the flux lies in the radio core, which

was not detected in early radio maps. This led to initial uncertainty about the optical identification; Jenkins, Pooley & Riley (1977, hereafter JPR) show four candidate objects, and their object b, a 19th magnitude galaxy, is suggested by Riley, Longair & Gunn (1980) to be the most likely on the grounds of its appearance and proximity to the radio centroid. Radio observations by Hiltner et al. and our new maps confirm that object b is indeed the host galaxy. Hiltner et al. give a red magnitude of 19.15 ± 0.05 . 3C 20 appears to be the dominant galaxy of a small group, although the field is crowded (Rawlings 1987). The centre of the host galaxy is elongated, and de Koff et al. (1996) consider it a candidate for an optical jet.

The redshift of 0.174 for 3C 20, given by Lawrence et al. (1986), is confirmed by observations by Laing (private communication).

Our A-configuration observations were made at observing frequencies of 8.4 and 8.7 GHz and a bandwidth of 12.5 MHz; the data from this were merged with the B- and C-configuration data sets without correction for spectral index (negligible in this case). The long track at A array gives very good uv -plane coverage, although the phase stability was poor over the later parts of the run due to snow. 3C 20 has a high integrated rotation measure, so polarization vectors may be misaligned with the true magnetic field direction by rotations of order 10° .

The low-resolution map in Fig. 1 shows the extended wings of the source, which is nearly as wide as it is long; the western lobe

Table 4. Properties of the images of FR II objects.

Source	Fig. number	Region	Method	FWHM		σ_I	σ_P	Dynamic range
				(arcsec)	(kpc)	(μ Jy)	(μ Jy)	
3C 20	1	Whole	C	1.10	4.39	63	19	4400
	2	Hot spots	CM	0.22	0.88	21	15	4900
3C 79	3	Whole	C	1.90	10.13	30	8	2700
	4	Hot spots	CM	0.24	1.28	13	14	800
4C 14.11	5	Whole	C	2.40	10.92	25	14	1200
	6	Core	C	0.70	3.185	18	–	1600
	7	Hot spots	CM	0.23	1.05	18	14	1600
3C 123	8	Whole	C	0.85	4.03	260	47	8600
	9	Whole	C	0.23	1.09	115	30	3900
	10	Hot spots	C	0.05	0.24	320	–	300
3C 132	11	Whole	C	0.50	2.34	38	12	1300
	12	Whole	C	0.80	3.74	75	–	800
	13	Hot spots	CM	0.22	1.03	33	9	1200
3C 153	14	Whole	C	0.26	1.46	39	14	3000
3C 171	15	Whole	C	0.70	3.54	55	18	2800
	16	Hot spots	CM	0.35×0.25	1.52	73	19	1300
	17	<i>HST</i> overlay	CM	0.35×0.25	1.52	73	19	1300
3C 173.1	18	Whole	C	1.70	9.91	27	13	1500
	19	Hot spots	CM	0.30×0.20	1.45	28	26	330
3C 234	20	Whole	C	2.30	9.61	58	16	2500
	21	Hot spots	CM	0.30	1.25	29	22	1200
	22	E hotspot	CM	0.50	2.09	27	–	1400
3C 284	23	Whole	C	3.60	18.29	22	16	1800
	24	Hot spots	CM	0.90	3.76	22	13	820
3C 300	25	Whole	C	2.10	11.68	33	–	4600
	26	Hot spot	C	0.23	1.29	38	60	340
	27	Core	C	0.23	1.29	38	60	340
3C 319	28	Whole	C	2.20	9.48	22	10	1000
	29	N hotspot	CM	0.90	3.88	22	13	800
3C 349	30	Whole	C	1.80	8.15	28	11	5000
	31	Hot spots	CM	0.25	1.13	28	22	900
3C 381	32	Whole	C	1.60	6.00	66	20	3200
	33	Hot spots	C	0.25	0.94	20	14	1900
3C 401	34	Whole	C	0.50	2.23	18	8	1600
	35	Whole	CM	0.27	1.20	28	22	1100
3C 436	36	Whole	C	2.20	10.32	24	11	900
	37	Hot spots	CM	0.23	1.08	16	22	1000
3C 438	38	Whole	C	0.50	2.91	25	10	700
	39	Whole	C	0.23	1.34	26	13	600

Column 4 gives the deconvolution method. C denotes CLEAN and CM denotes a CLEAN/MEM hybrid as described in the text. Columns 5 and 6 give the angular and corresponding linear size of the FWHM of the restoring beam used, or the major and minor axes where it was elliptical. In columns 7 and 8, σ_I and σ_P are the rms off-source noise on total and polarized intensity maps respectively. In several cases there are artefacts around bright hotspots at several times this level. The dynamic range (column 8) is defined as the ratio between the peak intensity and σ_I .

apparently bends north and the eastern lobe south. The edges of the lobes nearest the parent galaxy are highly polarized. At high resolution (Fig. 2) the jet in the western lobe (W1, W2) can be seen; the inner part (W1) is associated with a ridge of high polarization with the magnetic field perpendicular to the jet direction, but the magnetic field is parallel to the jet direction further out (W2). A possible counterjet feature in the eastern lobe (E1) is also highly polarized. The part of the jet nearest the host galaxy is resolved, but the area where the jet appears to undergo an S-bend is clearly seen. At both ends of the source a single compact ‘primary’ component can be identified. The primary in the eastern hotspot (E2) is elongated roughly towards the radio core and only weakly polarized; the bridge towards the more diffuse secondary (which actually contains two reasonably compact components, E3 and E4, which are not separate enough to count as multiple hotspots) is

strongly polarized with the magnetic field direction being along its length. One of the components in this region, E5, is separate enough to count as a distinct object by the definition of L97. In the western hotspot, the situation is more complicated. The unresolved (or barely resolved) primary W3 has an inferred magnetic field direction pointing approximately towards the ‘tail’ to the north and west; the ‘tail’ then has its magnetic field directed along its length, before turning to a perpendicular configuration at the peak (W4) at its end. To the east of the end of the tail the field is parallel to the source axis. This might well be interpreted as a version in miniature of the situation at the eastern end, with a primary hotspot and outflow to a secondary, W4 (although W4 is not separate from W3 by the definition of L97); the tail would then represent the continued flow after the primary shock. A couple of facts confuse this simple picture. The first is the presence to the south of the primary of a

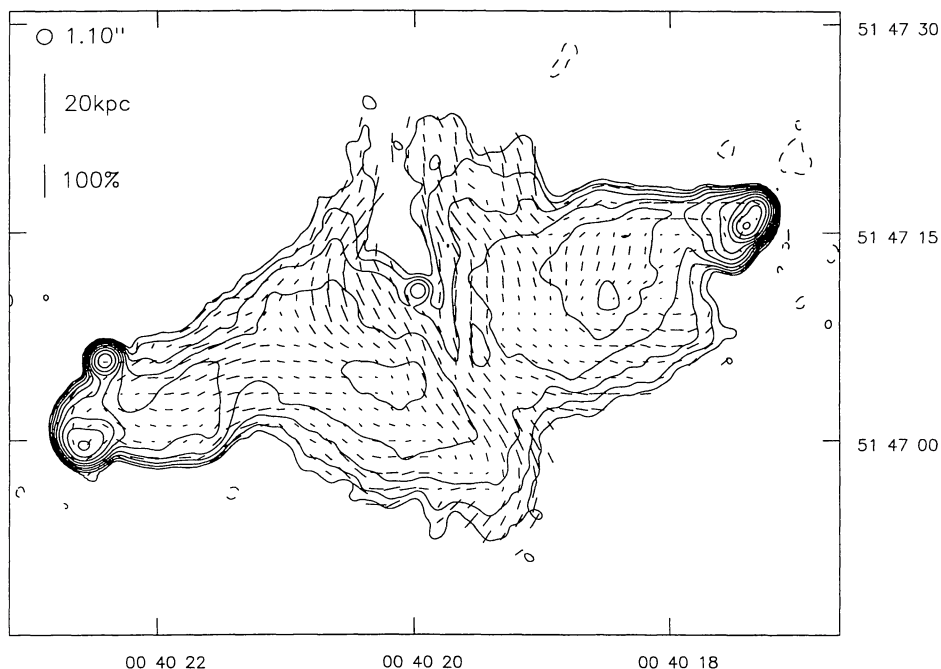


Figure 1. 3C 20 at 1.10-arcsec resolution. Contours at $0.25 \times (-2, -1, 1, 2, 4, \dots)$ mJy beam $^{-1}$.

further bright region (W5), sufficiently separate to count as a hotspot, not apparently connected to the primary but, like the secondary at the end of the tail, extending back into the western lobe. In the simple primary–secondary picture, this must be a defunct hotspot no longer being supplied with energy. Unfortunately the Hiltner et al. (1994) spectral index maps have no signal in this region. The second fact is the direction of the jet: where it is clearly seen it is pointing directly towards W4, so that to retain a simple picture with the beam terminating at the primary we need to propose another bend in the beam path over the 10 kpc or so between the jet’s disappearance on the radio map and the primary hotspot W3.

4.2 3C 79

3C 79 has been observed at a number of radio frequencies in spectral index studies, because of its high-surface-brightness lobes. In one of these Stephens (1987), using several frequencies, was able to produce ‘age maps’ showing that contours of constant age are concave towards the nucleus; this is consistent with a model in which the advance speed of the hotspots is greater than the speed of the backflow.

3C 79’s host galaxy has been classified as an N-galaxy with $R = 17.47$ (Sandage 1973); N-galaxies normally have broad emission lines (Grandi & Osterbrock 1978) and so 3C 79 might have been assumed to be a broad-line radio galaxy. Laing (private communication) fails to detect any broad wings on the $H\alpha$ line with a high-quality spectrum, so we have classified 3C 79 as a narrow-line object. The *HST* image shows no compact nucleus (de Koff et al. 1996), and so the classification as an N-galaxy may have been erroneous.

The galaxy may have one or two close companions (Taylor et al. 1996). A broad-band optical image by McCarthy, Spinrad & van Breugel (1995) is unremarkable, but their image in the 500.7-nm [O III] line shows an extended region of gas to the north-west which the western lobe appears to flow around. At sub-arcsecond

resolution the nuclear regions are complex and there is some alignment with the radio structure (de Koff et al. 1996).

The core of 3C 79 appears to have varied by about 5 mJy, an increase of 70 per cent, between the epochs of observation of our A- and B-array and the C- and D-array data. This was corrected for by subtraction from the A- and B-array data sets. A 1-mJy confusing source 75 arcsec to the north-east of the pointing centre has been removed from the map.

Our low-resolution map of 3C 79 (Fig. 3) shows the asymmetrical nature of the source. The western lobe is extended well to the south of the source axis, while the eastern lobe is more normal in shape. Both lobes have the unusual feature that the hotspot areas protrude in bottle-neck fashion from much broader lobes: compare 3C 234 and to a lesser extent 3C 132 and 3C 381 (see below). The lobes are not smooth: there is some evidence for structure in them even in the lower-quality maps of Spangler et al. (1984) and more is seen here. The bright region to the west of the hotspot in the eastern lobe, identified by Spangler et al. as a secondary hotspot, can also be seen clearly (E1). The source has no jets.

At high resolution (Fig. 4), both hotspot regions are revealed to have complicated multiple structure. The eastern end of the source comprises four separate components. The most compact is the south-eastern one (E5), which is slightly resolved and appears extended to the north and west; the magnetic field is directed roughly north–south. To the north of this is a less compact component, E4, extended southwards and north-westwards; to the north-west of this and joined to it by a bridge is a still more extended component, E3. A linear feature leaves this to the south-west and then appears to turn north-west, at E2, before disappearing; it points towards the extended region E1 which forms Spangler et al.’s ‘secondary hotspot’. It is tempting to regard this sequence of more and more diffuse hotspots, connected by ridges of emission, as also being connected by real ongoing outflow; in this model the most compact hotspot would be the site of termination of the beam (invisible here) and the rest, with the possible exception of the very diffuse secondary E1, would be successive sites of outflow redirection

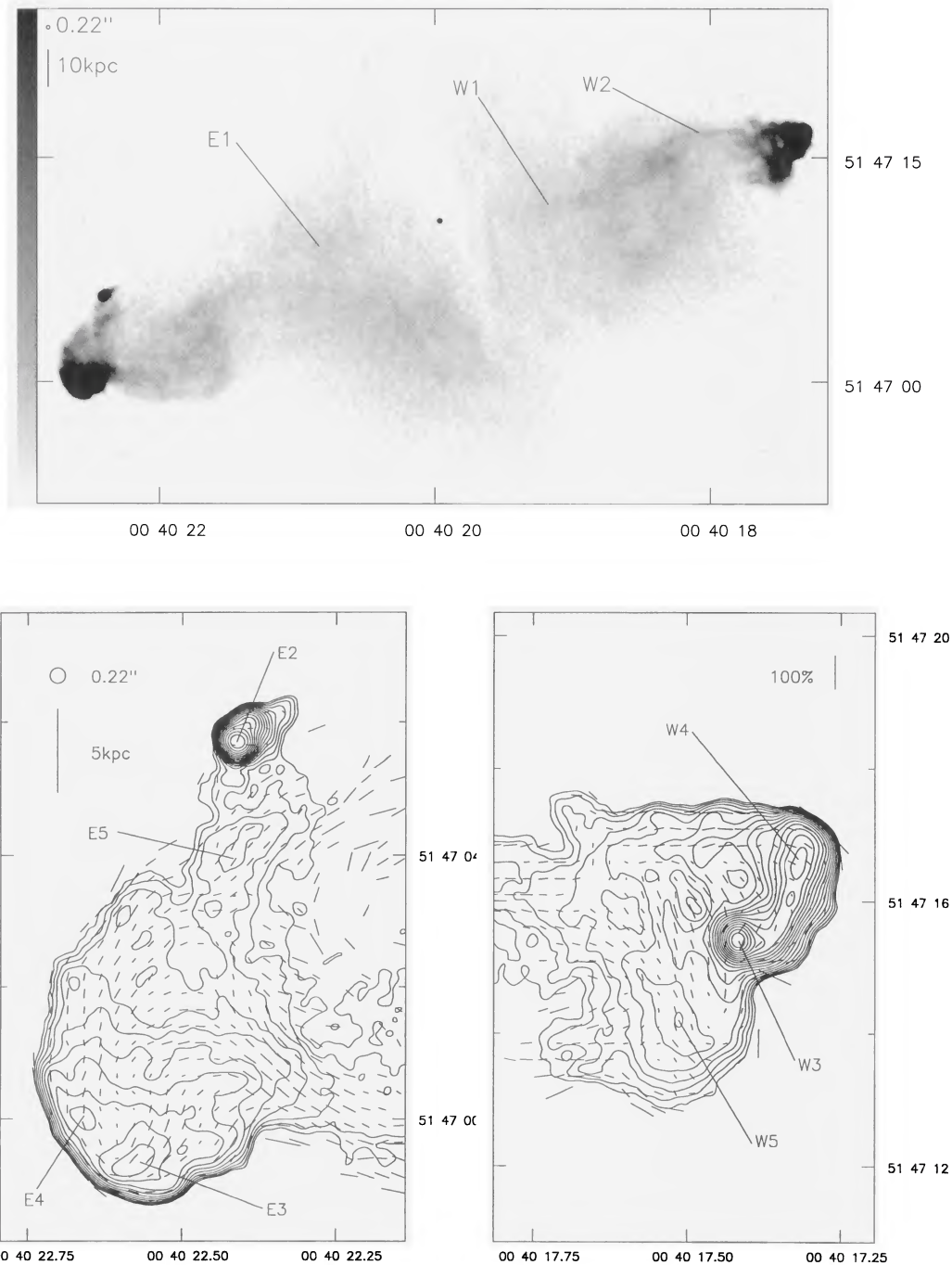


Figure 2. 3C 20 at 0.22-arcsec resolution. Above: linear grey-scale; black is 1 mJy beam⁻¹. Below left: eastern hotspot; contours at $0.2 \times (-\sqrt{2}, -1, 1, \sqrt{2}, 2, 2\sqrt{2}, \dots)$ mJy beam⁻¹. Below right: western hotspot, contours as left.

and decollimation. The directions of the magnetic field vectors are points in favour of this model: in the compact components they are perpendicular to the presumed flow, as might be expected if deceleration were occurring here; elsewhere they are parallel to it.

The situation is not quite as complicated in the western hotspot complex, which consists of three compact components. In this case the relative degrees of compactness are not easy to determine by eye, but Gaussian fitting shows that the southern component (W1) is the most compact. It is extended northwards by a bent ridge of emission which leads into the second most compact component, W2; this in turn is extended northwards and connects to the northern and most diffuse component, W3. This is extended eastwards into a

region of complicated structure which is strongly polarized with the magnetic field directed along the source axis. By analogy with the eastern hotspot region, we might suggest that the most compact hotspot (the southernmost one) is the current site of beam termination, and that the connections between it and the others and the magnetic field structures imply continued outflow between them.

4.3 4C 14.11

The core of 4C 14.11 varied over our observation period. The fluxes measured by fitting a Gaussian plus baseline to the maps with AIPS task JMFT are shown in Table 5. We corrected for this by adding to

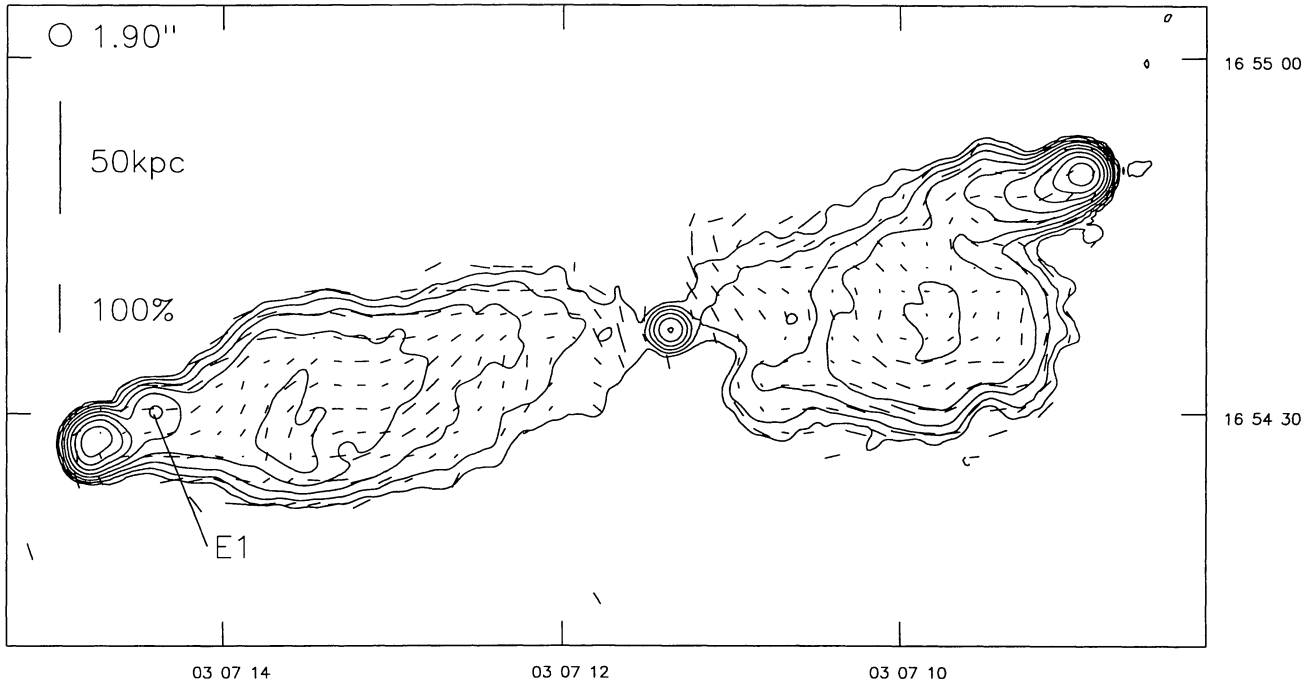


Figure 3. 3C 79 at 1.90-arcsec resolution. Contours at $0.20 \times (-2, -1, 1, 2, 4 \dots)$ mJy beam $^{-1}$.

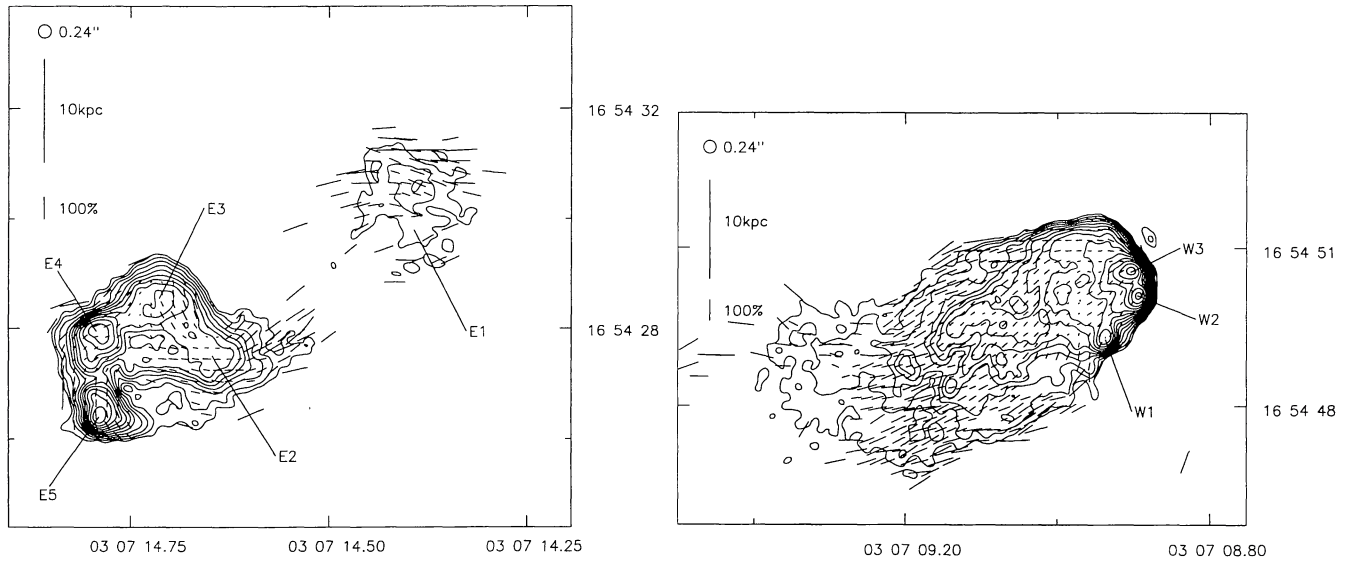


Figure 4. 3C 79 at 0.24-arcsec resolution. Left: eastern hotspot; contours at $0.1 \times (-\sqrt{2}, -1, 1, \sqrt{2}, 2, 2\sqrt{2}, \dots)$ mJy beam $^{-1}$. Right: western hotspot, contours as left.

and subtracting from the uv data so as to make all the fluxes the same as that of the A configuration.

The low-resolution map in Fig. 5 shows the multiple hotspots in both lobes. A curving filament leads out of the eastern hotspot complex into the lobe. The southernmost hotspot in the western hotspot complex is joined to the other two components visible at this resolution by a bridge of emission. There is a faint compact knot (E1) about 20 kpc to the south-east of the core. The lobes both extend to the north-east close to the host object, and the extended areas are highly polarized.

At high resolution the knot E1 is seen to be a linear feature 2.8 arcsec in length and unresolved transversely, aligned with the axis between the hotspots and the core. Fig. 6 shows an intermediate-

resolution map of this feature, which we have classed as a jet. The eastern hotspot (Fig. 7) consists of four components, of which one (the northernmost: E2) is clearly the most compact (it is slightly resolved in an east-west direction). At this resolution it can be

Table 5. The core flux of 4C 14.11.

Date	Flux (mJy)
1993/08/03	20.9 ± 0.3
1993/11/27	31.1 ± 0.5
1994/06/23	33.1 ± 0.2
1995/08/06	28.9 ± 0.1

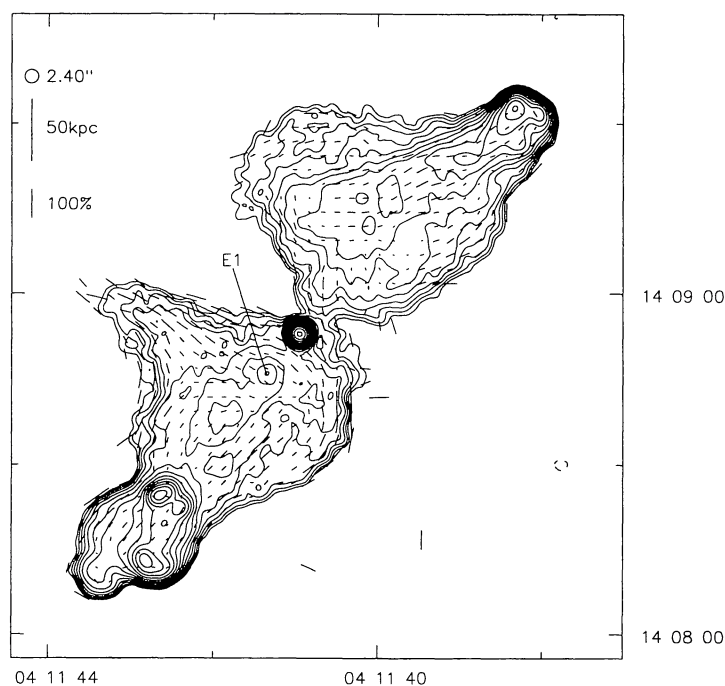


Figure 5. 4C 14.11 at 2.40-arcsec resolution. Contours at $0.15 \times (-\sqrt{2}, -1, 1, \sqrt{2}, 2, 2\sqrt{2}, \dots)$ mJy beam $^{-1}$.

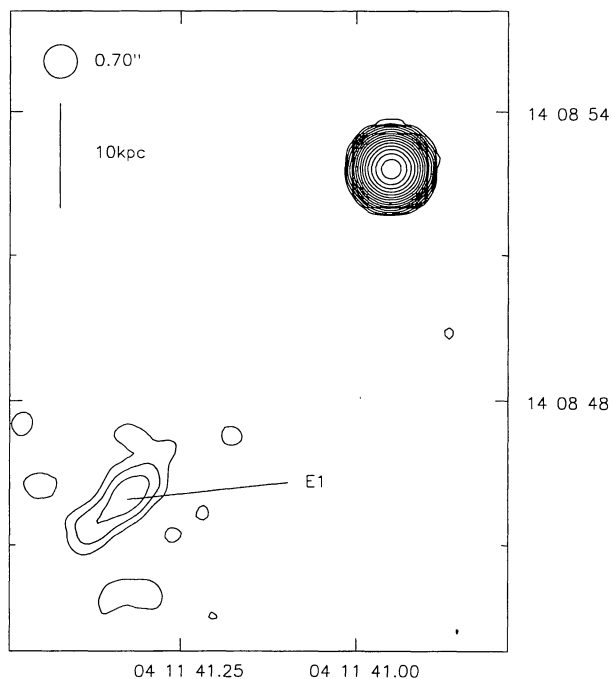


Figure 6. 4C 14.11 core and jet at 0.70-arcsec resolution. Contours at $0.18 \times (-\sqrt{2}, -1, 1, \sqrt{2}, 2, 2\sqrt{2}, \dots)$ mJy beam $^{-1}$.

distinguished from the component E3 to the south-east which is well resolved in position angle 45° . On the low-resolution map, these two appear as a single hotspot. To the south-west of this feature is another, E4, extended north-west–south-east, pointing towards the southernmost ‘hotspot’, E5, which was resolved even on the low-resolution map and which turns out to contain no compact structure at all. (It looks very like an extended, dimmer version of E3.) All these features have their magnetic fields in the direction of their longer axis.

It is not clear what the fluid flow is doing in this part of the source. E2 is the most compact hotspot, and so presumably the beam termination, but there is no evidence that it is ‘feeding’ E3. The diffuse components E4 and E5 resemble an old jet segment/hotspot pair which are no longer being powered by the beam.

In the western lobe the picture is simpler. There is only one truly compact hotspot, W2, and it is elongated transverse to the presumed beam direction, with magnetic field aligned along its length. The ridge line of the hotspot complex then connects it to a more diffuse region, W1 – approximately 10 kpc in size – whose magnetic field direction is transverse to a line drawn between its centre and that of the compact hotspot. This is consistent with a picture in which outflow is taking place from the compact to the less compact hotspot and thence out into the source via the curving filament described above.

Spectral index mapping between 8.4 and 1.4 GHz shows the hotspots to be the areas of flattest spectrum, as expected; the minima in spectral index ($\alpha \approx 0.7$) correspond to our identifications of the beam-termination hotspots (W2, E2). The entire south-eastern end of the source has a reasonably flat spectrum ($\alpha \approx 0.8$) and this, along with the multiple hotspots, might be taken as an indication that the beam has terminated further forward in the recent past. The spectral index elsewhere in the source steepens considerably transverse to the source axis; there is little evidence for a significant gradient *along* the axis.

4.4 3C 123

3C 123 is associated with an $R = 18.94$ magnitude galaxy with strong Galactic reddening. An optical CCD image given by Hutchings, Johnson & Pyke (1988) shows the galaxy to have a good deal of diffuse structure to the south and south-west of the nucleus, and Hutchings (1987) suggests that this may be the result of galaxy interaction. There are many faint small objects in the field, so the object may be part of a cluster (Longair & Gunn 1975; Rawlings 1987), although *Einstein* detected no X-ray source associated with

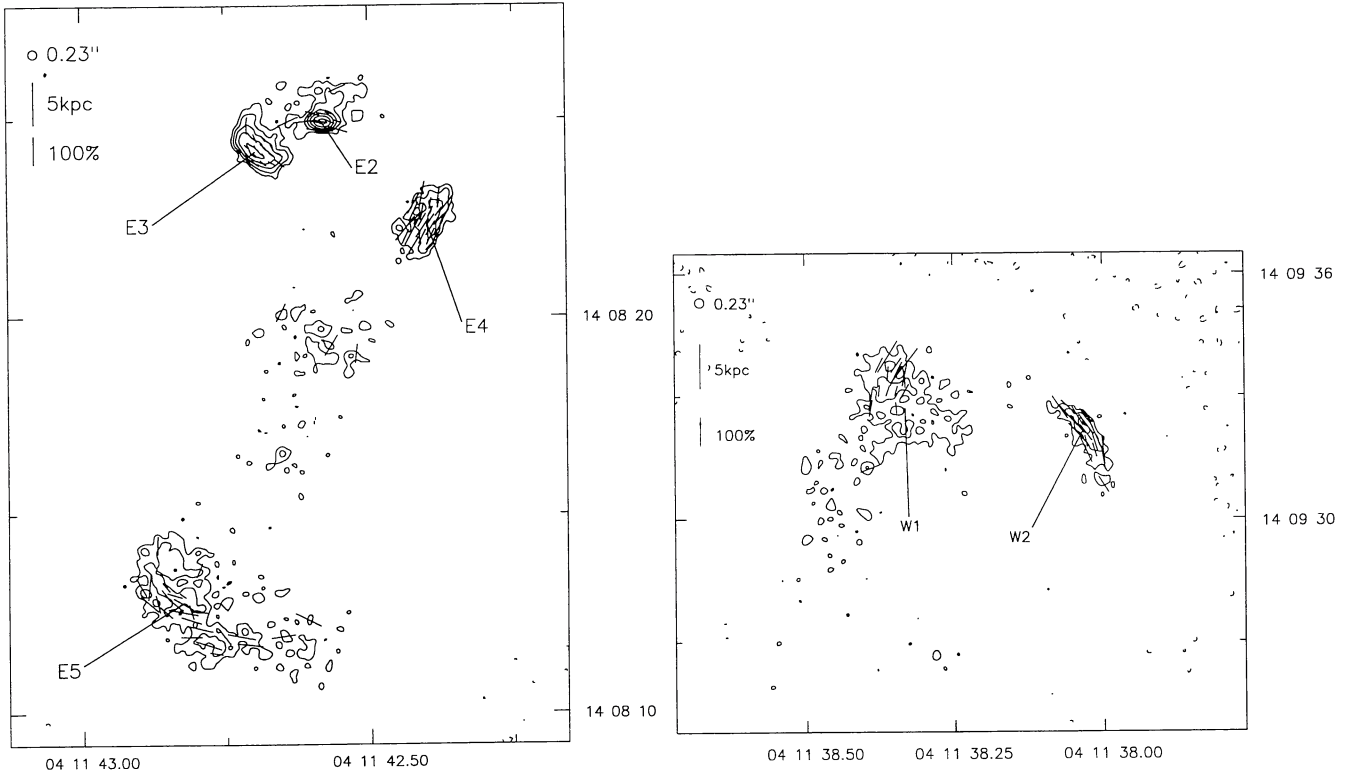


Figure 7. 4C 14.11 at 0.23-arcsec resolution. Left: eastern hotspot; contours at $50 \times (-2, -1, 1, 2, 4, \dots) \mu\text{Jy beam}^{-1}$. Right: western hotspot; as left.

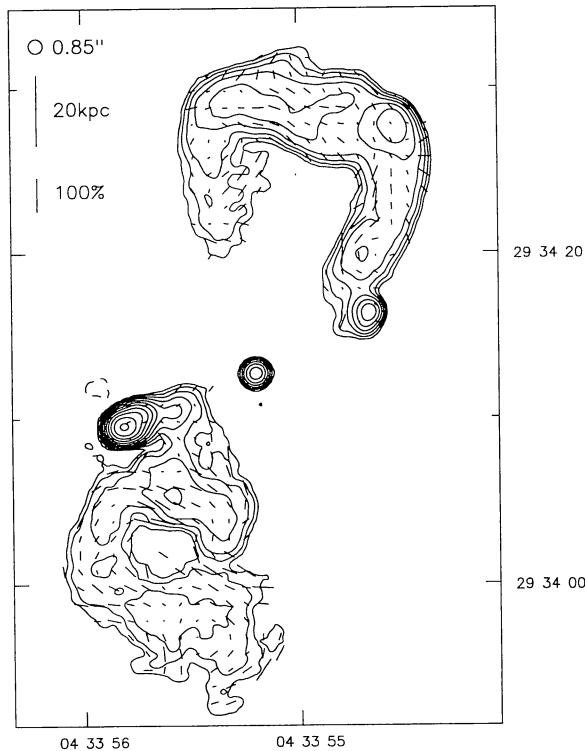


Figure 8. 3C 123 at 0.85-arcsec resolution. Contours at $2 \times (-2, -1, 1, 2, 4, \dots) \text{mJy beam}^{-1}$.

the radio galaxy (Rawlings 1987). On the basis of the weak lines seen by Laing (private communication), we have classified it as a low-excitation object; it is possible, however, that the reddening misleadingly biases the $[\text{O III}]$ flux and that it should be classified as a NLRG.

The rotation measure of 3C 123 is large and negative, probably due to the Galactic material that reddens the host in the optical. It lies in a region of the sky where many sources have large negative RM. Polarization vectors at 8 GHz may thus be misaligned with the true magnetic field direction by rotations of order 25° . Attempts to assess the RM variation across the source using 5-GHz data available to us suggest that there may be variations in RM with respect to the mean of order 100 rad m^{-2} across the source, but variations of this order should not affect the polarization too badly.

A low-resolution map (Fig. 8) reproduces the structure seen by Cox et al. (1991). The polarization of the source follows the curves of the plumes well, with the magnetic field being consistently aligned along the plumes. (The fractional polarization map is made with points five times the rms noise in the polarization and total intensity maps, as the noise near the source is dominated by artefacts from the deconvolution of the bright hotspot.)

The detailed structure of the hotspots (Fig. 9) is as unusual as that of the rest of the source. Both are double, but the eastern hotspot complex is extremely bright (over 4 Jy at 8.4 GHz). At the highest 8-GHz resolution it can be seen to consist of two components, the brighter (E4) being resolved while the dimmer (E3) contains an unresolved component. Both are extended east-west and their magnetic fields are, largely speaking, directed along this axis. Neither points towards the core. However, there are some knots (E1, E2) to the west of E3 which might trace the bending of a beam. Apart from these there is no indication of a jet at this resolution. The western hotspot complex is more normal: at 0.23-arcsec resolution the southern one, W1, is unresolved and the northern one, W2, is

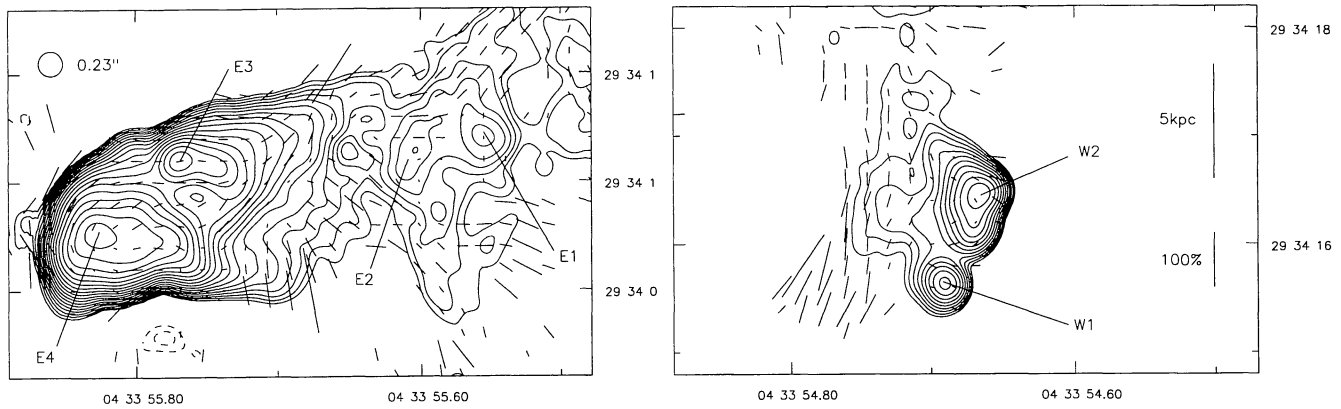


Figure 9. 3C 123 at 0.23-arcsec resolution. Left: eastern hotspot; contours at $1 \times (-\sqrt{2}, -1, 1, \sqrt{2}, 2, 2\sqrt{2}, \dots)$ mJy beam $^{-1}$. Right: western hotspot; contours as left.

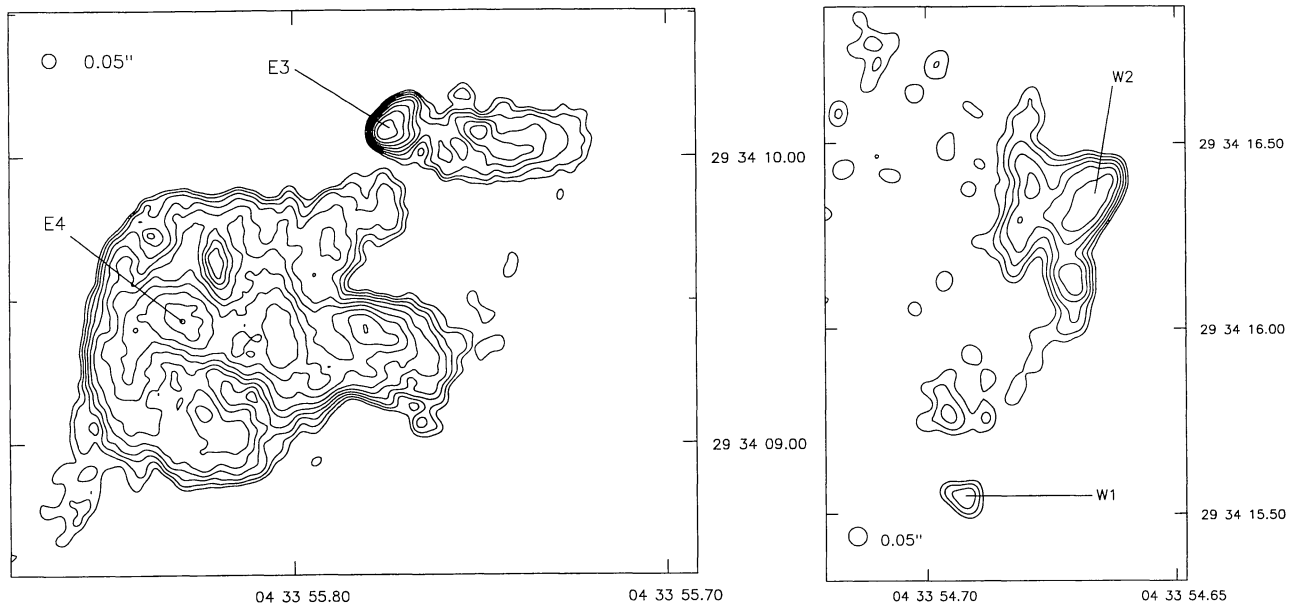


Figure 10. 5-GHz images of 3C 123 at 0.05-arcsec resolution. Left: eastern hotspot; contours at $2 \times (-\sqrt{2}, -1, 1, \sqrt{2}, 2, 2\sqrt{2}, \dots)$ mJy beam $^{-1}$. Right: western hotspot; contours at $1 \times (-\sqrt{2}, -1, 1, \sqrt{2}, 2, 2\sqrt{2}, \dots)$ mJy beam $^{-1}$.

extended north–south. Both hotspots have a comparatively low degree of polarization.

We obtained 5-GHz MERLIN observations of 3C 123 (consisting of one 16-h run on 1995 June 27 in multi-frequency mode, with observing frequencies of 4.55, 4.86 and 5.18 GHz) to investigate the structures in the hotspots further. These (Fig. 10) provide three times the resolution of Laing’s 15-GHz images in Cox et al. (1991), although a lack of short baselines means that structure on scales larger than 3.5 arcsec is not seen; the images are noisy as a consequence, since much of the flux of 3C 123 is on these scales. At this resolution E3 is resolved, showing a cylindrical shape with a length of around 3 kpc and a bright head (at the eastern end) whose size is around 0.7 kpc; a knot further back in the tail is distinct by the definition of L97. E4 is fully resolved into an east–west line of three knots, at least two of which are distinct according to L97’s definition, with bright filaments branching off them to north and south. The ‘pits’ of very low emission separating these filaments appear to be real, although they might be filled in to some extent by shorter-baseline data. The ‘mushroom-cap’ shape of the eastern end of E4 is suggestive of a bow shock. The whole complex is remarkably reminiscent of the western hotspots of Cygnus A

(e.g. Perley & Carilli 1996), with the E3 hotspot corresponding to hotspot B in Cygnus A (it shows the same head–tail structure) and E4 corresponding to hotspot A. However, an understanding of the fluid flow in the source remains elusive. E3 must be identified, on the criteria we have used, as being the primary hotspot; but does its tail trace the incoming beam, or is it outflow into the lobe? Carilli, Dreher & Perley (1989) argue that the corresponding feature in Cygnus A west – the tail of hotspot B – traces flow into the secondary, but it is difficult to see how this might be happening in 3C 123. On the other hand, the brightness (and corresponding energy density) of E4 argues that it must have been connected to the beam until very recently, if it is not still being supplied with power. In favour of a model in which E4 is a disconnected former primary and E3 the new site of beam termination is their similarity in shape: it is not hard to imagine E4 as an inflated version of E3, possibly with some inflow and outflow still going on as in the models of Cox et al. (1991). W2 and W1, by contrast, appear to be a normal double hotspot pair very like those in the other sources. W1 is clearly the primary, and there is evidence in the MERLIN image for flow between W1 and W2, and between W2 and the lobe (to the north and east). The fact that the two ends of the source are so

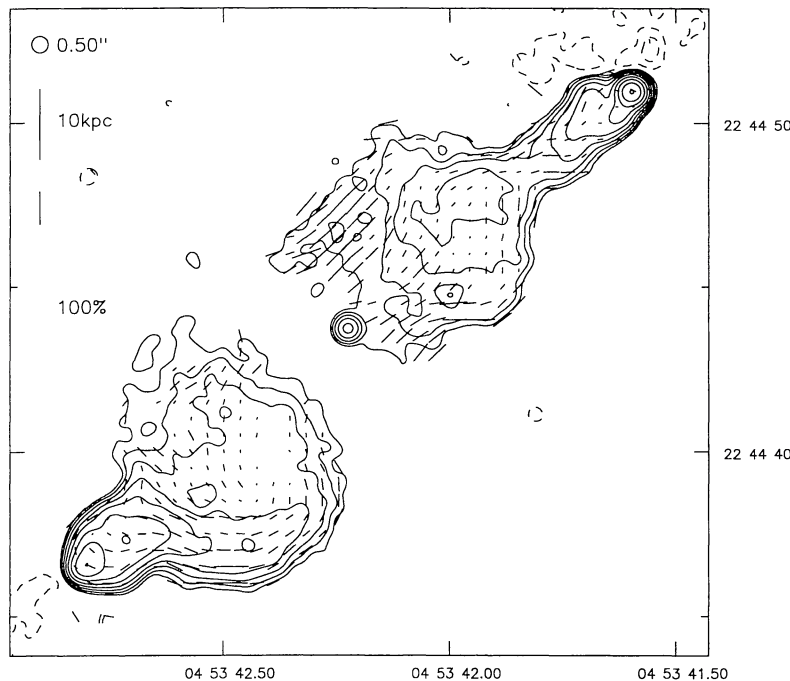


Figure 11. 3C 132 at 0.50-arcsec resolution. Contours at $0.2 \times (-2, -1, 1, 2, 4 \dots)$ mJy beam $^{-1}$.

different in their structure and inferred fluid flow means that a model explaining the hotspot brightness asymmetry in terms of relativistic beaming is difficult to sustain; it is more likely that the environments of the two hotspots are significantly different.

These observations shed a little light on the reasons for the peculiar large-scale structure of 3C 123. First, the hotspot structures, although the eastern one is unusual, are understandable when compared with other objects and with theoretical models. 3C 123 is therefore an ordinary classical double source behaving in a peculiar way, rather than being something entirely unique. Two possible models remain to be distinguished. The first, initially proposed by Riley & Pooley (1978), is that the beam axis has precessed over the lifetime of the source, and that this together with projection is sufficient to explain its structure. The second is that the source axis has remained constant, but that outflow from the hotspots has formed plumes rather than lobes, in a manner similar to that proposed for 3C 171 below (Section 4.7) and presumably caused by an unusual large-scale environment. These models are distinguishable in principle with sufficiently high-resolution spectral age determinations, since, in the first, regions of equal age in the two lobes should be connected by a straight line passing through the core; while, in the second, assuming no re-acceleration and similar outflow speeds, regions of equal age should be at similar distances from the hotspots. However, the necessary observations would be extremely difficult. [The spectral index observations of Stephens (1987) are not of sufficiently high resolution to be used for this purpose.] The well-collimated and almost constant-width appearance of the plumes is a challenge for both models, but particularly for the precession model. The multiple nature of the hotspots has been adduced as evidence for beam precession (Cox et al. 1991), but multiple hotspots are now seen to be common; the fact that the primaries are in the correct positions for ongoing precession (in a north-through-west sense on the maps shown) is equally consistent with an outflow model. The fairly good alignment of the magnetic field with the plume axes (except at the very ends of the plumes) seems more consistent with a model with ongoing outflow. This

field configuration is similar to that of the plumes of wide-angled tail sources. The final argument against precession, and so by implication for a model involving outflow, is simply the amount of precession required: the beam axis would have to change direction by at least 70° over the lifetime of the source (a few $\times 10^6$ yr). With the possible – and debatable – exception of the winged sources (e.g. Leahy & Williams 1984), precession of this magnitude on these time-scales has not been observed or inferred for any other classical double source; by contrast, many sources exhibit peculiar structures which can be attributed to an unusual environment. These arguments lead us to favour the outflow model. The question of what might be special about the environment of 3C 123 remains open, however.

4.5 3C 132

Our map shows a radio core and so confirms JPR's identification of the source with a 19th magnitude red galaxy. The host galaxy is imaged by Hutchings et al. (1988) and is classed by Hutchings (1987) as an interacting irregular; there are several faint objects within a few arcseconds of the host galaxy. Some structure is observed in its centre (de Koff et al. 1996). There is, however, no clear relationship between the radio and optical alignments.

The data set used to make our images needs a small amount of shorter-baseline data to sample the source completely. The result of the undersampling is a slight negative 'bowl' around the source.

3C 132 is an ordinary classical double of small size (Fig. 11). Both hotspot regions, but particularly the northern one, protrude in bottle-neck fashion from broader lobes, as seen in 3C 79 and 3C 234. The eastern lobe has an unusual brightening along its southern edge, starting at the hotspot and extending around the lobe, which might be interpreted as backflow. At slightly lower resolutions (Fig. 12) there is the suggestion of a linear feature (E1, E2) which appears to run from close to the core to the bright edge of the hotspot region. We have classified it as a possible jet. High-resolution maps (Fig. 13) resolve the hotspot areas. The western hotspot, W1, has a size of

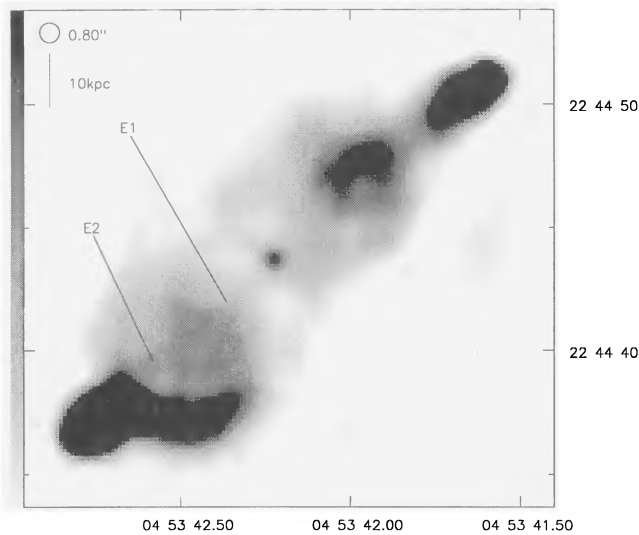


Figure 12. 3C 132 at 0.80-arcsec resolution. Linear grey-scale: black is 5 mJy beam⁻¹.

about 800 pc, and the eastern one, E4, is extended on scales of about 2 kpc. Both hotspots have inferred magnetic fields transverse to the source axis. A curving feature leaves the western hotspot to the south-east and then bends north-east about 7 kpc away from the hotspot before terminating in a diffuse region; this might also be interpreted as backflow. A diffuse component of the eastern head, E3, is separate enough to count as a hotspot by the definition of L97.

4.6 3C 153

Hutchings et al. (1988) have imaged the host galaxy of 3C 153, a $V = 18.5$ mag elliptical, but remark only that it is too small to note any structure. *HST* observations (de Koff et al. 1996) show an elliptical nucleus. Rawlings (1987) suggests that the environment is a cluster.

Our maps (Fig. 14) show the southern lobe of 3C 153 to be reasonably similar to those seen in larger sources. It has a clear

double hotspot, one component of which (W3) is barely resolved (Gaussian fitting suggests a size of 0.5 kpc); the other, W2, is much more diffuse and has a tail leading back into the lobe. The magnetic field is transverse to the presumed beam direction in W3 and is in the same direction in the line linking W3 and W2, turning through 90° in W2; this follows the pattern seen in the larger sources. The knot W1 at the base of the southern lobe is not the core, as it is extended along the source axis and has a spectral index between 1.7 and 8.4 GHz of around 0.6 [the flux at 1.7 GHz being estimated from the map of Lonsdale & Morison (1983)]; instead it is probably a tracer of the path of the beam. No core is detected; from estimates of the on-source noise and the confusing flux we can say that its flux must lie below about 0.5 mJy at 8.4 GHz.

The northern lobe is unusual in being broader than it is long and containing a hotspot, E2, which is located at the centre of the lobe rather than the leading edge. The hotspot is resolved and appears elongated approximately transverse to the source axis. The magnetic field in the lobe is transverse to the axis almost everywhere. The linear extension of the lobe towards the south-west, E1, is real [it appears on the map of Lonsdale & Morison (1983) and that of Neff et al. (1995)]. It lies on the straight line between E2 and W3 which also goes through W1 in the southern lobe and the optical identification position, and may be another tracer of the beam. We have therefore classed 3C 153 as having two possible jets. The unusual structure of the northern lobe is almost certainly due to a complicated local environment; the source lies largely inside its parent galaxy.

4.7 3C 171

The host galaxy of 3C 171, an $R = 17.94$ mag object, is imaged by Hutchings et al. (1988) in the optical; it shows considerable elongation along the axis of the radio jets. This is even clearer in an *HST* snapshot (de Koff et al. 1996) but may well be due to contamination of the optical passbands by line emission; there is no evidence for this elongation on a UKIRT *K*-band image (Best, private communication). Heckman et al. (1984) have shown convincing evidence for an interaction between the radio-emitting

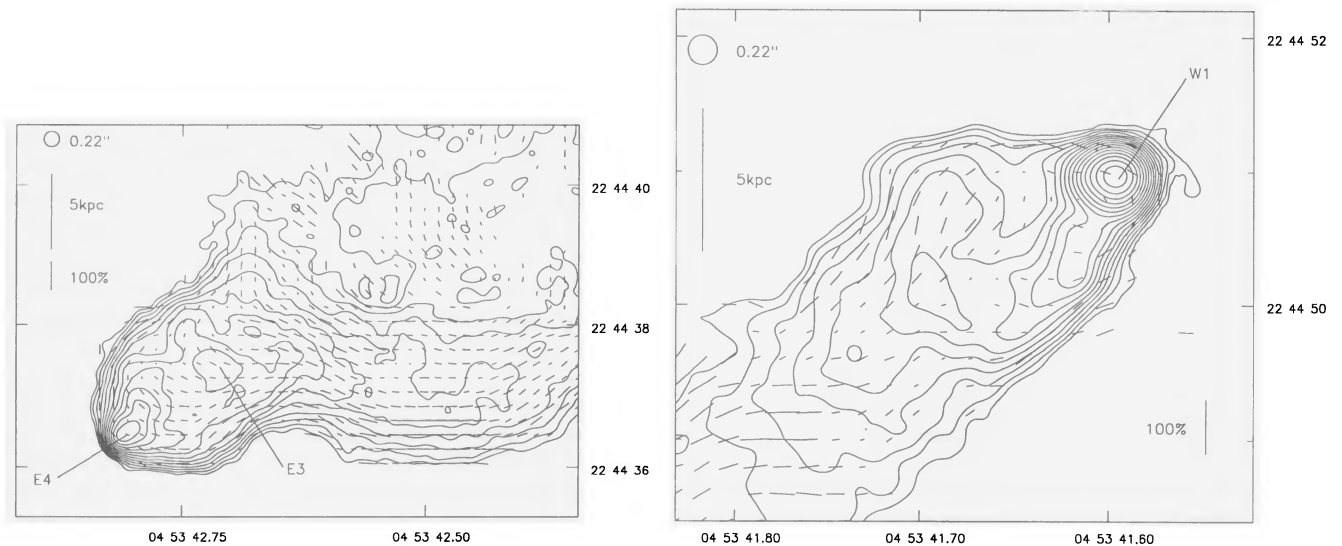


Figure 13. 3C 132 at 0.22-arcsec resolution. Left: eastern hotspot; contours at $0.15 \times (-\sqrt{2}, -1, 1, \sqrt{2}, 2, 2\sqrt{2}, \dots)$ mJy beam⁻¹. Right: western hotspot; contours as left.

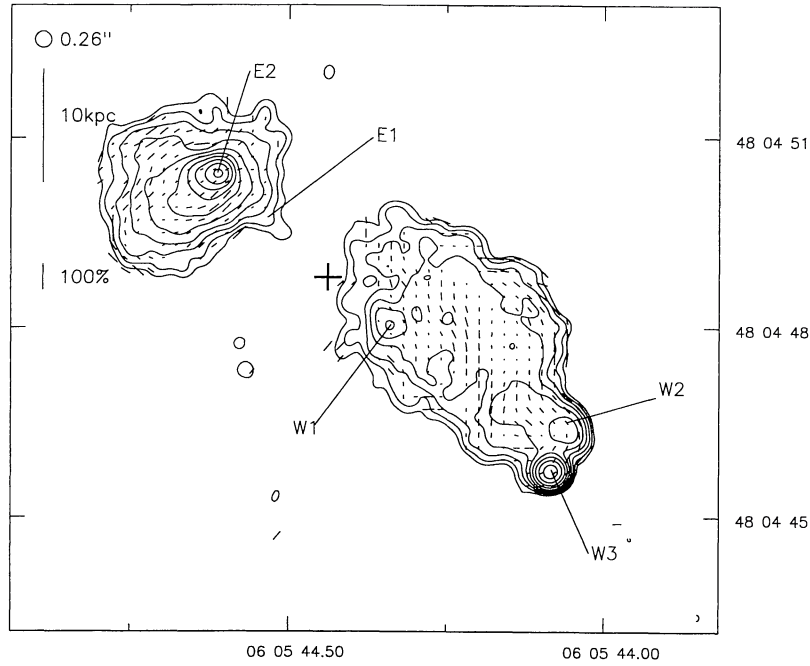


Figure 14. 3C 153 at 0.26-arcsec resolution. Contours at $0.2 \times (-2, -1, 1, 2, 4, \dots)$ mJy beam $^{-1}$. The position of the optical identification is marked with a cross.

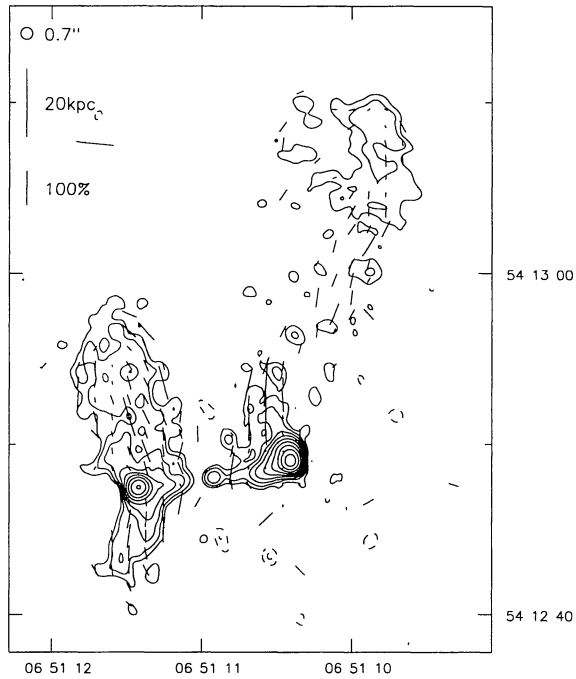


Figure 15. 3C 171 at 0.70-arcsec resolution. Contours at $0.4 \times (-2, -1, 1, 2, 4, \dots)$ mJy beam $^{-1}$.

plasma and the extended emission-line regions in the source. The emission-line regions are brightest just beyond the hotspots.

The observations of Laing et al. (1994) and Eracleous & Halpern (1994) show 3C 171 to be a narrow-line radio galaxy in spite of its classification by Smith, Spinrad & Smith (1976) as an N-galaxy. Wyndham (1966) lists the object as an ordinary red galaxy, but its colour in Sandage (1973) is sufficient to put it in the section of parameter space normally occupied by N-galaxies. If 3C 171 really is an N-galaxy, it (like 3C 79, above) does not follow the strong

trend noted by Grandi & Osterbrock (1978) for N-galaxies to be broad-line objects. It is likely, however, that the situation has been confused by the unusual continuum structure seen in the *HST* image of de Koff et al. (1996). The nucleus in that image is resolved, suggesting that the object is not an N-galaxy after all.

Poor *uv*-plane coverage at A configuration means that we have had to use an elliptical restoring beam (0.35×0.25 arcsec in position angle 75°) at the highest resolution. A low-resolution map (Fig. 15) shows the main unusual features of the source: bright hotspots, twin jets and extended plumes transverse to the source axis. The sampling on the shortest baselines is poorer than is usual for this study and so the details of structures in the plumes should not necessarily be believed. At high resolution (Fig. 16), the jets in both lobes (E1, W1) can clearly be seen. The hotspots are both slightly resolved, and extensions from the hotspot areas into the lobes can be seen on both sides. The western hotspot, W2, is only weakly polarized, but the eastern hotspot, E2, is completely unpolarized; in fact, a whole strip of the eastern jet and lobe, passing through the hotspot, has almost no polarized emission. This is related to the line-emitting material associated with the jet, as can be seen in Fig. 17, which shows an overlay of the radio map on the *HST* snapshot of de Koff et al. Not only does the optical material appear to be associated with the jets, but also the polarization is clearly closely related to the optical material. The 0.5-kpc-wide strip in the eastern lobe with no polarization is precisely cospatial with the optically emitting material, while the western hotspot is clear of optical emission and has some polarized flux.

Laing (1981) suggests that the object is related to the class of wide-angled tail sources (WATs: Burns 1985), and the resemblance is certainly striking up to a point: both have twin inner jets and bright hotspots. However, 3C 171's lobes are very different from the well-collimated plumes of a typical WAT, and the eastern lobe extends both north and south. There is no evidence that the host of 3C 171 is a dominant cluster galaxy, and no detection in the X-ray. It seems likely that the jets of 3C 171 disrupt not because they undergo reconfinement somewhere in the galactic environment, but because

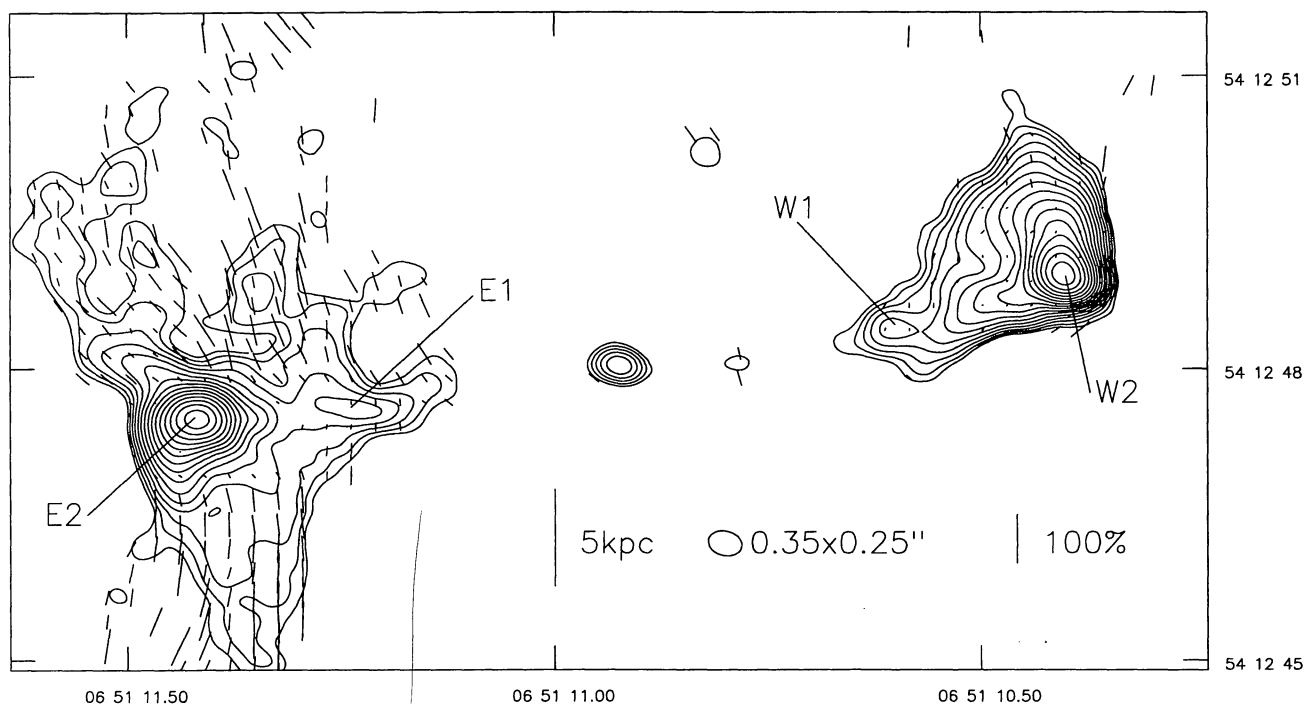


Figure 16. 3C 171 at 0.35×0.25 arcsec resolution. Contours at $0.4 \times (-\sqrt{2}, -1, \sqrt{2}, 2, 2\sqrt{2}, \dots)$ mJy beam $^{-1}$.

they are interacting with the cold dense material traced by the optical line emission. If so, it is not surprising that the direction of the outflow from the hotspots is unusual; 3C 171 may be treated as an ordinary FR II whose lobes are disrupted in an unusual way, and is perhaps comparable in this respect to 3C 123.

4.8 3C 173.1

The host galaxy of 3C 173.1 lies in a poor cluster (Eales 1985b; de Koff et al. 1996). The nuclear continuum emission is aligned north-south approximately along the axis of the jet (de Koff et al. 1996).

Poor uv -plane coverage at A configuration means that we have had to use an elliptical restoring beam (0.30×0.20 arcsec in position angle 75°) at the highest resolution.

3C 173.1 is one of the more ordinary sources in the sample. A low-resolution map (Fig. 18) shows the jet in the northern lobe (N1), first detected by LP; this can clearly be distinguished from lobe material at intermediate resolution (not shown). The jet is obscured by a region of high surface brightness (N2) on the western side of the northern lobe; this is linked to the hotspot region by a bridge of emission.

At high resolution (Fig. 19) the northern hotspot is seen to consist of three components. The westerly component, N5, is the most compact – it is just resolved at this resolution – and has magnetic field roughly transverse to its direction of extension. A faint and marginally less compact second component N4, just separate from N5, is to the east, and the most diffuse component, N3, is on the eastern edge of the source, with magnetic field alignment approximately north-south. The bridge described above leads from this hotspot into the lobe. The images are consistent with N3 being fed from N5/N4. It is interesting, however, that the jet when last seen is pointing towards N3 rather than N5.

The southern hotspot again has multiple sub-structure, though none of the components is distinct by the definition of L97. The brightest point is a resolved but reasonably compact hotspot S1,

elongated transverse to the source axis, and to its west is a curving ridge of emission S2. To the south-west of these and joined to them there is a diffuse bar of emission (S3), whose relation to the other components is unclear. The hotspots, and indeed this whole region of emission, have their magnetic field direction transverse to the source axis.

Spectral index mapping shows that the region of high surface brightness N2 has a flatter spectrum ($\alpha \approx 0.9$) than the material immediately to its west ($\alpha \approx 1.2$). This may be further evidence for collimated backflow in this source. The material with the steepest spectrum is that at the edges of the lobes where they are closest to the nucleus, as expected from simple models of spectral ageing.

4.9 3C 234

3C 234's host is an N-galaxy with $R = 16.52$ which appears to be located on the edge of a small group of fainter galaxies of similar size (Eales 1985a,b). It was detected in the X-ray by the *Einstein* satellite (Feigelson & Berg 1983). The host galaxy was imaged by Hutchings et al. (1988) who noted four small, red close companion objects. An *HST* continuum image of the nuclear regions (de Koff et al. 1996) shows extension to the east and west; in particular, there is a curved region of emission extending 2 arcsec to the west. This may be due to emission-line contamination.

Antonucci's (1982) discovery that 3C 234 has broad lines which are strongly polarized perpendicular to the radio axis (together with a strongly polarized featureless continuum in the optical) has made it the canonical example of a 'hidden quasar' in models for radio galaxy-quasar unification (e.g. Antonucci 1993). The implication is that it is nearer the plane of the sky than a true broad-line object.

Our maps (Fig. 20) show 3C 234 to be the most striking example of the 'bottle-neck' lobe structure found in this sample (compare 3C 79). Its lobes are broad at their base but are connected to the hotspots by well-collimated necks of emission (150 kpc long and only 35 kpc across in the eastern lobe). The magnetic field in the necks is

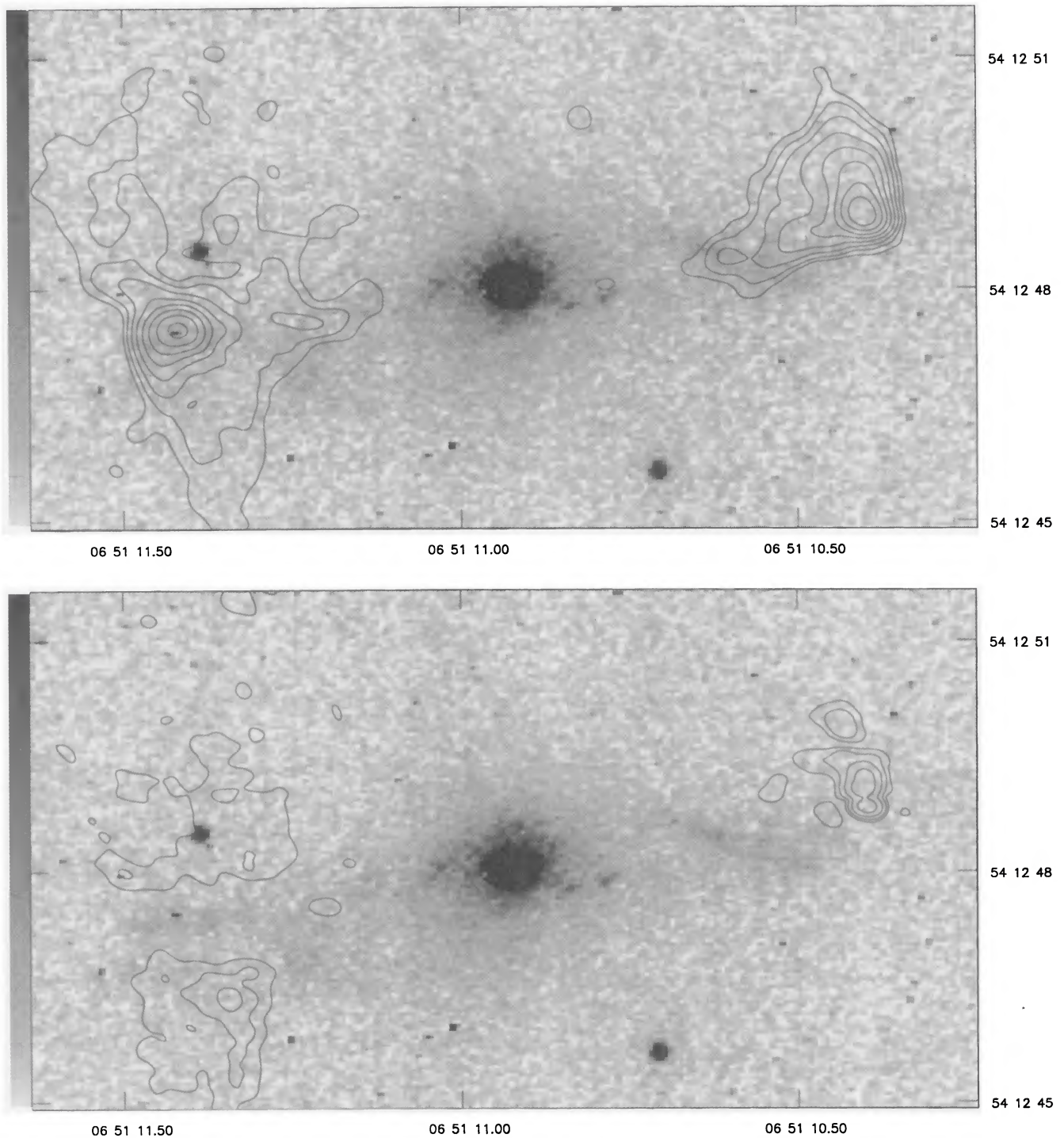


Figure 17. 3C 171 at 0.35×0.25 arcsec resolution overlaid on an *HST* snapshot. The grey-scale is in arbitrary units. Above: contours of total intensity at $0.4 \times (-2, -1, 1, 2, 4 \dots)$ mJy beam $^{-1}$. Below: contours of polarized intensity at $0.2 \times (-2, -1, 1, 2, 4 \dots)$ mJy beam $^{-1}$.

parallel to the source axis; in the bases of the lobes it is largely transverse. The eastern lobe shows a secondary hotspot, E2, very like that seen in the eastern lobe of 3C 79; there is also some evidence for a jet, in the form of a faint linear feature (E1) passing through the broad faint lobe before disappearing into the neck. The neck in the western lobe is unusual in appearing to be bent through about 20° from the axis of the rest of the source.

At the full resolution available (Fig. 21), the eastern hotspot shows complicated structure, as discussed by Dreher (1981). The

most compact component, E5, is clearly resolved, and is extended in position angle 107° . Perpendicular to the direction of extension (slightly west of south), a bright knotty ridge E4 leaves the hotspot and extends back into the lobe, curving as it does so. This ridge is real, and is readily distinguishable in intermediate-resolution maps both in polarized intensity (this is clear in the lower-resolution maps of Zukowski 1990) and in total intensity (Fig. 22); it seems most likely that it is a tracer of the beam (particularly as the ridge E1 points at that edge of the lobe), and we have classed it as a jet. If it is

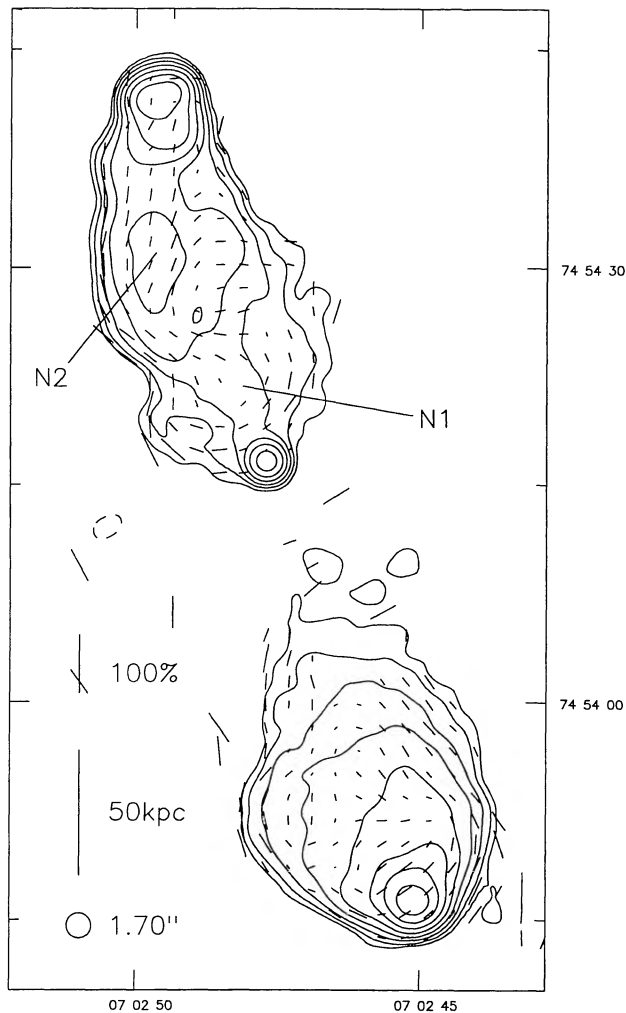


Figure 18. 3C 173.1 at 1.70-arcsec resolution. Contours at $0.2 \times (-2, -1, 1, 2, 4, \dots)$ mJy beam $^{-1}$.

a jet, the beam has to bend through some 35° in the 8 kpc or so immediately before the hotspot. E5 has magnetic field transverse to its direction of extension; E4 has a longitudinal field. A 'tail' of emission, E3, which is not separate from E5, leaves E5 parallel to its direction of extension and then seems to bend south towards a faint component E6. It is not obvious whether E2 is still connected to the fluid flow; where polarization is detected in this component, the magnetic field is roughly parallel to the source axis.

The situation is simpler in the western hotspot. There is a single compact component, W1, extended roughly north-south and with magnetic field parallel to the direction of its extension. Ridges leave the hotspot on either side and bend back into the lobe, suggesting symmetrical outflow; one component of the northern ridge (W2) is a separate hotspot according to the definition of L97. There is no sign of an incoming jet.

4.10 3C 284

Eales (1985b) shows a CCD image of the field of 3C 284, which Rawlings (1987) suggests may contain some associated galaxies, and McCarthy et al. (1995) class as a moderately rich cluster. The nucleus of the host galaxy is roughly aligned with the radio axis (de Koff et al. 1996).

A low-resolution map (Fig. 23) shows few remarkable features. High-resolution maps (Fig. 24) reveal a double hotspot in the eastern lobe; this follows the pattern seen in other sources, in that the magnetic field direction of the most compact hotspot, E2, is transverse to the source axis while the field direction of the more diffuse one, E1, is more or less along the source axis. The hotspots appear to be joined by a bridge of emission. The western hotspot, W1, is extended in position angle -30° ; its magnetic field is roughly transverse to its direction of extension.

4.11 3C 300

3C 300 lies in a poor cluster (McCarthy et al. 1995). In the *HST* image of de Koff et al. (1996), the nucleus appears extended to the north-west.

The polarization information in our B and D configurations at 8.0 GHz was not well calibrated owing to problems with the observing run, and so low-resolution polarization maps are not shown. A polarization map made at a different frequency can be found in Blundell (1994).

A low-resolution map in total intensity (Fig. 25) shows the asymmetrical nature of the source. The bright eastern hotspot (Fig. 26) shows clear double structure at the highest resolutions, with one component (E3, at the western edge of the hotspot region) being extended towards the other, much brighter component (E2), which in turn is extended back towards the core. The two components are similar in size and lie in an area of high surface brightness, and both have magnetic field direction transverse to the source axis; it is not clear which is the current beam termination point, or what the relation is between this hotspot and the lobe to the south-west, which contains a region (E1) that could almost be counted a secondary hotspot in its own right. The jet in the western lobe, first detected by Blundell (1994), can be traced all the way from the core to the end of the lobe (W1-4), as the high-resolution image around the core (Fig. 27) shows. There is insufficient signal-to-noise ratio at the full resolution to see reliable details of the dim north-western end of the source, and an image is therefore not shown; but Gaussian fitting to maps at intermediate resolution suggests that there is some sub-kiloparsec structure at the tip of the source. The angle between the beam as traced by W1 in Fig. 27 and that terminating in E3/E2 is some 10° to 15° short of 180° ; the jet in the western lobe also appears bent. Some of the inferred bending in the beams may be related to the unusual environment implied by the east-west extended [O III] emission seen by McCarthy et al. (1995).

4.12 3C 319

Spectral index studies (e.g. Macklin 1983) show that 3C 319 is a classical double in spite of its one-sided appearance. The optical object coincident with the radio hotspot (e.g. Crane, Tyson & Saslaw 1983) has now been shown to be a chance superposition with a neighbouring galaxy (Keel & Martini 1995). The field of 3C 319 contains a number of faint red objects (JPR; Eales 1985b; Rawlings 1987), at least two of which have redshifts which show them to be associated with the source, and another two of which have colours consistent with being at the same redshift (Keel & Martini 1995).

Our low-resolution map of 3C 319 (Fig. 28) shows the features that make the source unusual: it has no core or southern hotspot. Unsurprisingly, no jet is detected. From the position of the optical

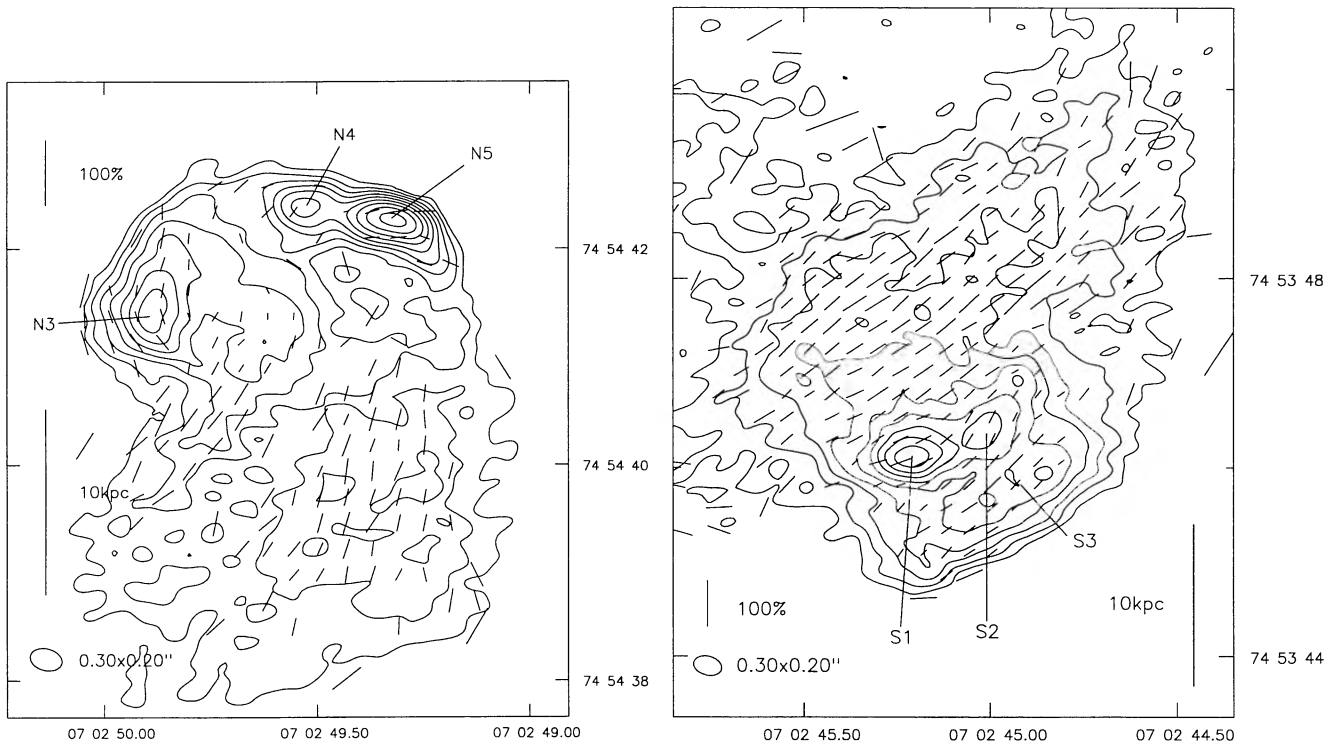


Figure 19. 3C 173.1 at 0.30×0.20 arcsec resolution. Left: northern hotspot; contours at $0.2 \times (-\sqrt{2}, -1, 1, \sqrt{2}, 2, 2\sqrt{2}, \dots)$ mJy beam $^{-1}$. Right: southern hotspot; contours as left.

identification it seems that the core, if it exists, should lie in the low-surface-brightness region at the centre of the source; the polarization behaviour of the lobes supports this. From an estimate of the on-source noise in this region we can say that the core is very unlikely to be brighter than 0.3 mJy. A high-resolution image (Fig. 29) shows that the hotspot, N1, is extended roughly along the source axis and has its magnetic field transverse to it. Fainter extensions leave the hotspot to the north-west and south-east.

4.13 3C 349

3C 349's host galaxy ($R = 17.84$) appears to have a close small companion (Eales 1985a,b).

A low-resolution map (Fig. 30) shows a reasonably ordinary source. There is a bright well-defined region of emission N1 in the middle of the northern lobe, connected to the hotspot by a ridge, and the end of the northern lobe has the bottle-neck shape seen in 3C 234 and 3C 79. At the end of the southern lobe a pronounced constriction in the lobe boundary (at S1) divides the hotspot region from the rest of the source; this type of feature occurs in a number of objects (e.g. 3C 135: L97). The magnetic field in the lobes is directed along the source axis except at N1.

The high-resolution maps (Fig. 31) point up the large differences between the brightnesses of the hotspot areas. The northern hotspot is largely resolved, with no bright structure visible on sub-kpc scales. The brightest component, N2, has its long axis transverse to the source axis and a tail – the precursor of the ridge described above – leads back into the lobe. The southern hotspot (S2), by contrast, clearly still has unresolved structure. It is extended and has its magnetic field direction transverse to the source axis. A diffuse bright region extends from the hotspot back into the lobe; a faint region to the east of S2 (S3) counts as a faint secondary hotspot. The only sign of a jet is a knot 4.5 arcsec south-east of the core, also

remarked upon by LP; in the high-resolution images it is seen to be extended along the source axis, but it is not long enough to be a jet according to the criteria of Bridle & Perley (1984). It has been classed as a possible jet.

Spectral index mapping between 1.4 and 8.4 GHz shows the expected spectral steepening along the source axis. In addition, correlations between spectral index and flux density changes are visible in both lobes. The spectrum steepens suddenly to the south-east of N1 and to the north-west of the constriction at S1.

4.14 3C 381

Wyndham (1966) classifies the host galaxy of 3C 381 as G(ND:), the only galaxy so classified, in contrast to his usual description of N-galaxies as N. He remarks that the galaxy appears 'almost stellar' on the red plate. This classification and identification appear to be the basis for Grandi & Osterbrock's (1978) classification of the source as an N-galaxy; they report weak broad H α in addition to a strong narrow component of the same line. It would appear, therefore, that neither the classification as an N-galaxy nor that as a broad-line object is particularly secure. The nucleus, in the *HST* image of de Koff et al. (1996), is similar to that of an ordinary elliptical.

3C 381's host galaxy lies in a small group, with a nearby companion, and is an $R = 16.86$ mag object. A broad-band image by McCarthy et al. (1995) shows the companion; their [O III] 500.7-nm image shows a separate linear feature which corresponds to the base of the 'bar' in the radio (see Fig. 32), providing direct evidence for interaction between the radio lobe material and emission-line gas. The *HST* image of de Koff et al. (1996) shows tails to the north and south of the optical nucleus.

A bright (40 mJy) steep-spectrum confusing point source lies 200 arcsec west of the pointing centre and was subtracted from our maps.

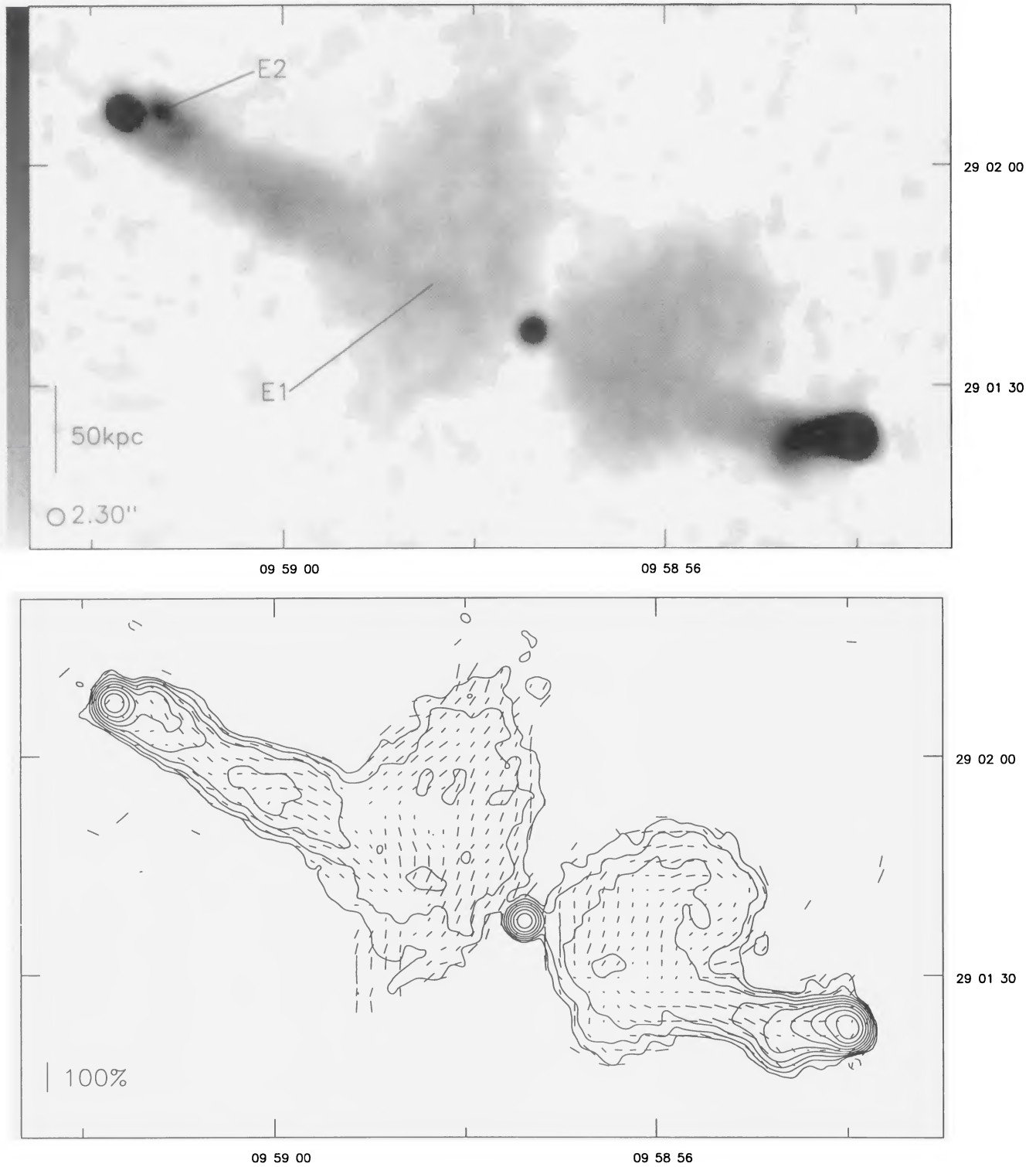


Figure 20. 3C 234 at 2.30-arcsec resolution. Above: linear grey-scale; black is 8 mJy beam^{-1} . Below: contours at $0.3 \times (-2, -1, 1, 2, 4, \dots) \text{ mJy beam}^{-1}$.

The low-resolution maps (Fig. 32) show a reasonably normal source whose most striking feature is the bright bar, N1, in the northern lobe. This is connected at its western end by a bridge to the hotspot, and appears to curve to the north again at its eastern end. As the bar is bounded to the south by a region of cool gas (see above), it is very difficult to interpret this feature in terms of anything other

than strong backflow. The magnetic field in the bar is parallel to its direction of extension.

The high-resolution map (Fig. 33) shows the very different natures of the two hotspots. The northern hotspot clearly has double substructure, with the more compact but weaker component, N2, to the south-west; this is unresolved at 0.25-arcsec resolution. The

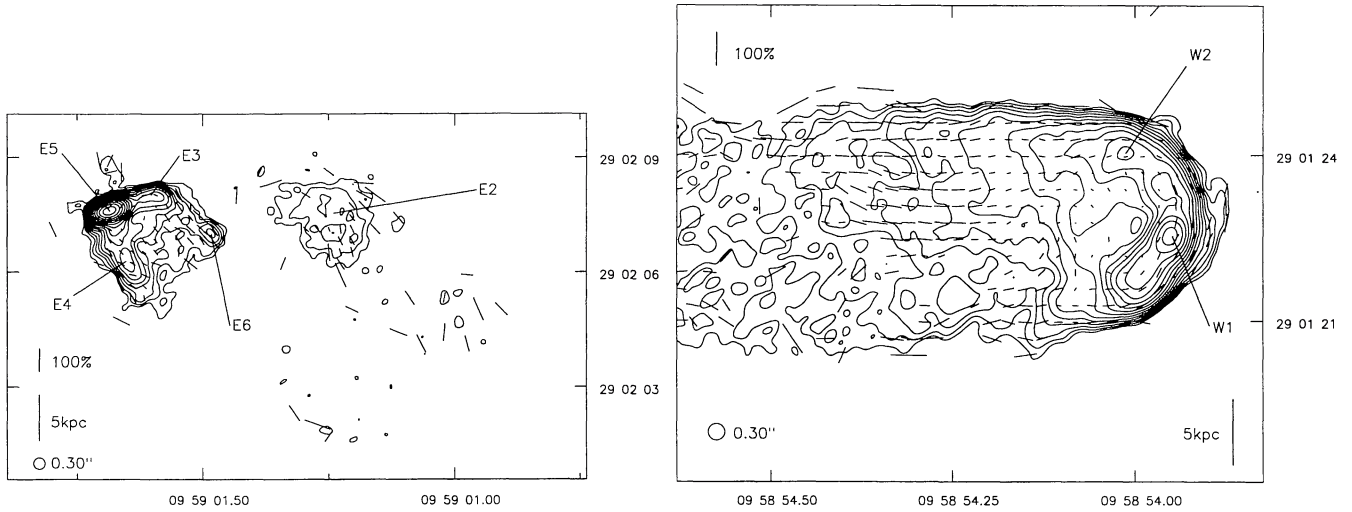


Figure 21. 3C 234 at 0.30-arcsec resolution. Left: eastern hotspot; contours at $0.15 \times (-\sqrt{2}, -1, 1, \sqrt{2}, 2, 2\sqrt{2}, \dots)$ mJy beam $^{-1}$. Right: western hotspot; contours as left.

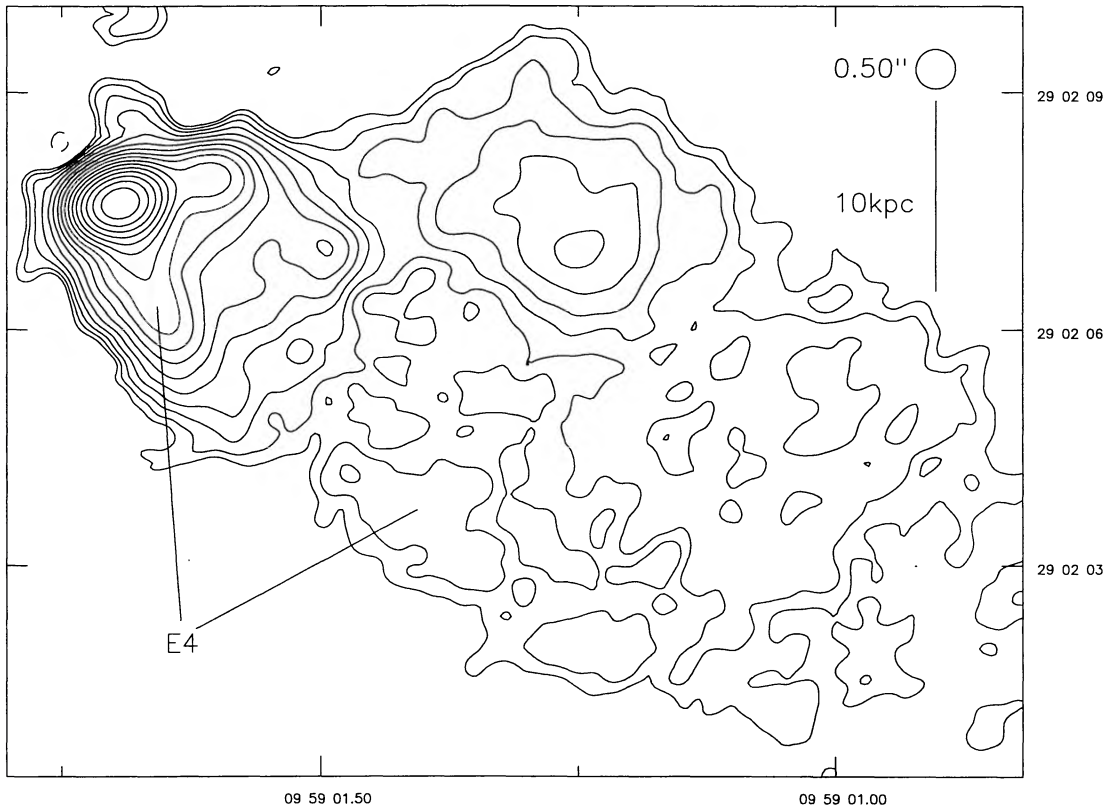


Figure 22. Eastern hotspot of 3C 234 at 0.50-arcsec resolution. Contours at $0.15 \times (-\sqrt{2}, -1, 1, \sqrt{2}, 2, 2\sqrt{2}, \dots)$ mJy beam $^{-1}$.

north-eastern component, N3, is slightly resolved and extended southwards. The magnetic field in N2 is in position angle 45° ; that in N3 varies along its length. Both components sit on a bright background region about 5 kpc across, and do not count as separate hotspots by the definition of L97. The extensions to the north-east and north-west are artefacts caused by the brightness of the hotspot region; the ridge which can be seen running southwards from the hotspot and then bending north-east is real, however, and may represent a change of direction for the backflow responsible for producing the bar. By contrast, the southern hotspot region appears to have no single compact component; a number of knots of similar

size are distributed throughout the hotspot region. The brightest is S1 but there are at least five separate components by the definition of L97. We might hypothesize that strong turbulence within the lobe has caused the beam to disrupt and distribute energetic particles over a wide region at this point in the source's lifetime, a phenomenon seen in numerical simulations (e.g. Hardee & Norman 1990); in this case a bright compact hotspot might well form again on timescales of a few thousand years.

The spectral index between 1.4 and 8.4 GHz shows little variation along the source, although the curving bases of the lobes appear to have considerably steeper spectra than the rest of it. The signal-to-

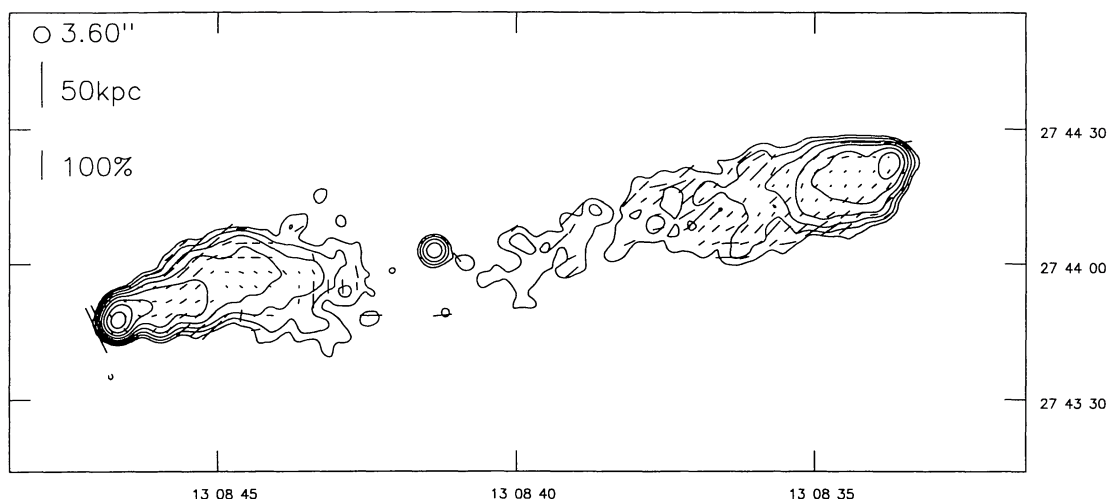


Figure 23. 3C 284 at 3.60-arcsec resolution. Contours at $0.2 \times (-2, -1, 1, 2, 4, \dots)$ mJy beam $^{-1}$.

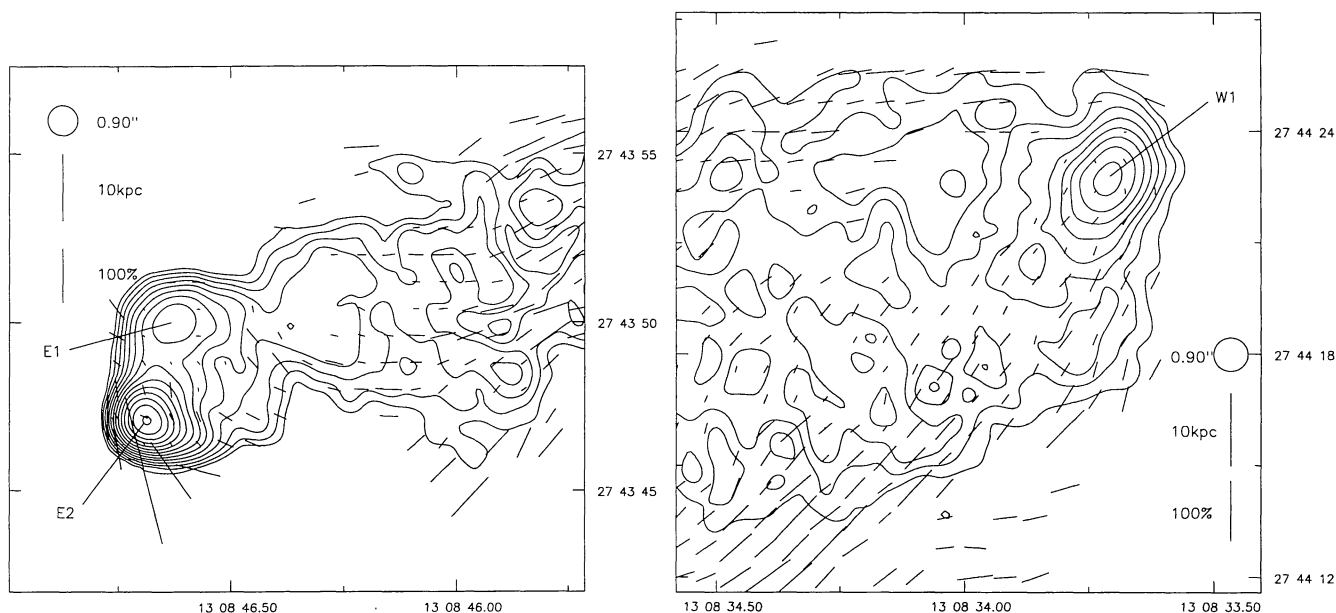


Figure 24. 3C 284 at 0.90-arcsec resolution. Left: eastern hotspot; contours at $0.2 \times (-\sqrt{2}, -1, 1, \sqrt{2}, 2, 2\sqrt{2}, \dots)$ mJy beam $^{-1}$. Right: western hotspot; as left.

noise ratio in our maps is insufficient to provide spectral information on the low-surface-brightness ‘wings’ seen by LP. There is some evidence that the spectrum of the bar in the northern lobe is flatter than that of the material immediately to the north of it; this is evidence either of compression or of re-acceleration in the bar.

4.15 3C 401

3C 401 is embedded in a faint diffuse region of X-ray emission (Feigelson & Berg 1983). The host galaxy appears double or interacting on the plate of Longair & Gunn (1975), and appears to lie in an optical cluster of Abell class 1 (Harvanek, private communication). The degree of polarization at low resolution and 2.7 GHz is unusually low (Laing 1981). These facts seem to indicate an unusual (and presumably unusually dense) environment for 3C 401. The integrated RM of 3C 401 is unknown, and so magnetic field directions should be inferred from the polarization vector directions with caution.

A low-resolution map of 3C 401 (Fig. 34) shows the jet in the

southern lobe that makes this source so unusual. The southern lobe also has an extension to the east, much like the proto-wings of 3C 381, which is highly polarized. Neither lobe has a compact hotspot. At the full resolution available (Fig. 35) the jet (S1) can be seen to be knotty, and bent at several places, and has inferred magnetic field parallel to its length (unlike the jets in FRIs) in contrast to the mainly transverse magnetic field configuration of the bases of the lobes. The jet can be traced into the ‘warm spot’ – approximately 10 kpc across – at the tip of the southern lobe (S2), with inferred magnetic field transverse to its direction of extension and to the direction of the incoming jet. There is no sign of a counterjet in the northern lobe, but there is again a ‘warm spot’ N1 with a tail that extends back towards the core. The resolved areas in both lobes with low or absent polarization are striking.

4.16 3C 436

The host galaxy of 3C 436 is an $R = 17.32$ object, with some fainter objects in the field. The nucleus shows dust features and appears to

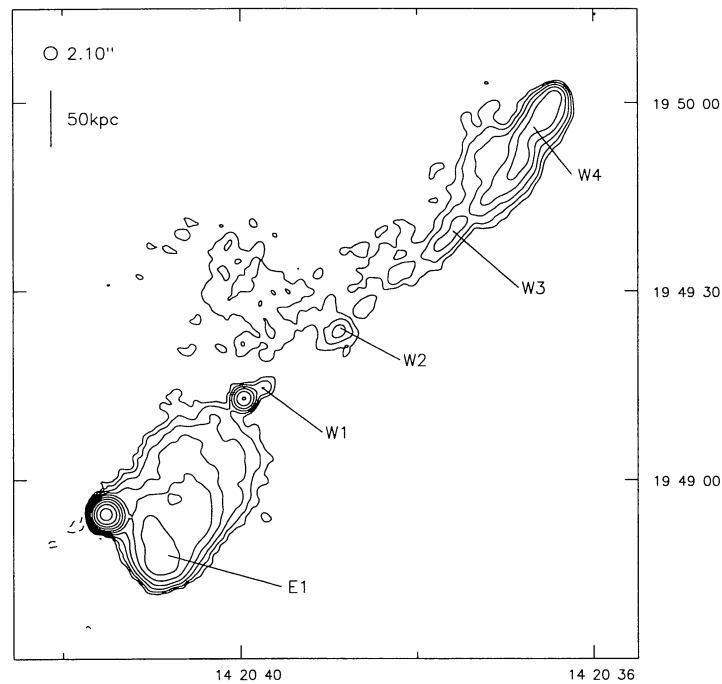


Figure 25. 3C 300 at 2.10-arcsec resolution. Contours at $0.2 \times (-2, -1, 1, 2, 4, \dots)$ mJy beam $^{-1}$.

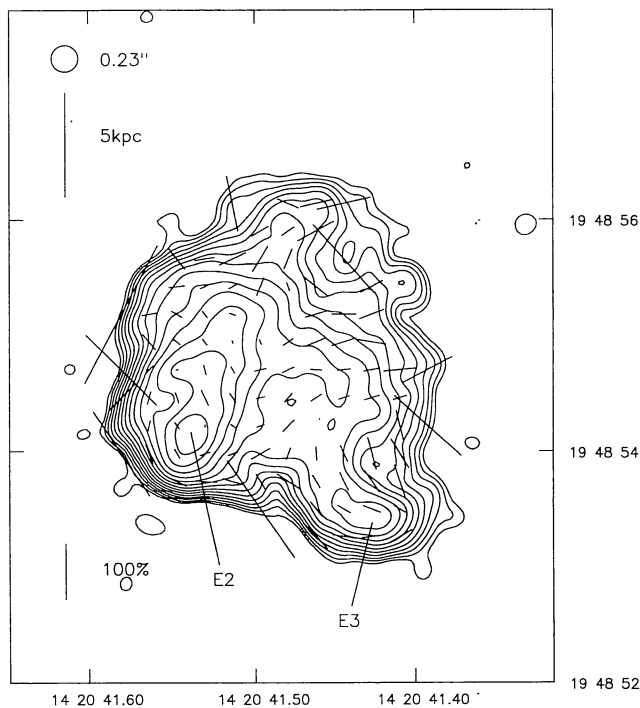


Figure 26. Eastern hotspot of 3C 300 at 0.23-arcsec resolution. Contours at $0.1 \times (-\sqrt{2}, -1, 1, \sqrt{2}, 2, 2\sqrt{2}, \dots)$ mJy beam $^{-1}$.

be aligned north–south (de Koff et al. 1996). A 3-mJy confusing source 110 arcsec to the north-west of the pointing centre has been removed from our maps.

The low-resolution map (Fig. 36) shows the main features of the source. The two lobes are symmetrical on the large scale, but there is a jet (S1, S2) and prominent double hotspot in the southern lobe while the northern lobe has weak hotspots and no jet. The jet appears to have transverse magnetic field, but its contrast with the

surrounding material is low, so this may not indicate the true field in the jet. There is no gap between the northern and southern lobes.

At the full available resolution (Fig. 37) the hotspots in the northern lobe (N1, N2 etc.) are barely visible above the noise: they evidently contain no bright structure on size-scales below a few kpc. By contrast, the southern lobe has a very compact hotspot, S3 (Gaussian fitting suggests a sub-kpc minor axis). This lies at the end of the jet, has magnetic field transverse to it, and is extended north and westwards. There is also a bright but diffuse secondary hotspot, S4, at the tip of the source. It is noteworthy that a jet that appears to be resolved, with a width of a few kpc, should produce such a compact hotspot. S4 has a magnetic field aligned along its direction of extension.

4.17 3C 438

3C 438 is well known to have bright twin jets (e.g. LP) on the basis of an unpublished snapshot by Laing. The source is completely unpolarized in the images of LP; Laing (1981) comments that the polarization is unusually low at 2.7 and 5 GHz (at low resolution), which may be an indication of a dense magneto-ionic environment. 3C 438 was detected in the X-ray with *Einstein* (Feigelson & Berg 1983) and is the brightest galaxy in a rich cluster (Longair & Gunn 1975); it seems to be a case, like 3C 401, of an unusually dense environment producing an unusual radio source. The integrated rotation measure of 3C 438 is not known [observations by Inoue et al. (1995) fail to constrain it well], so magnetic field direction must be inferred with caution from the vectors plotted.

A nearby bright (9 mJy) confusing point source was removed from our maps. The low-resolution map (Fig. 38) shows some of the extended structure seen in the map of LP. LP saw an extension of the northern lobe to the south-west which is not seen here; since the short baselines are well sampled, this implies that the far edges of the lobes have a very steep spectrum. The source is not strongly polarized even at this frequency (averaging about 10 per cent). The prominent jets are visible. The northern jet has inferred magnetic

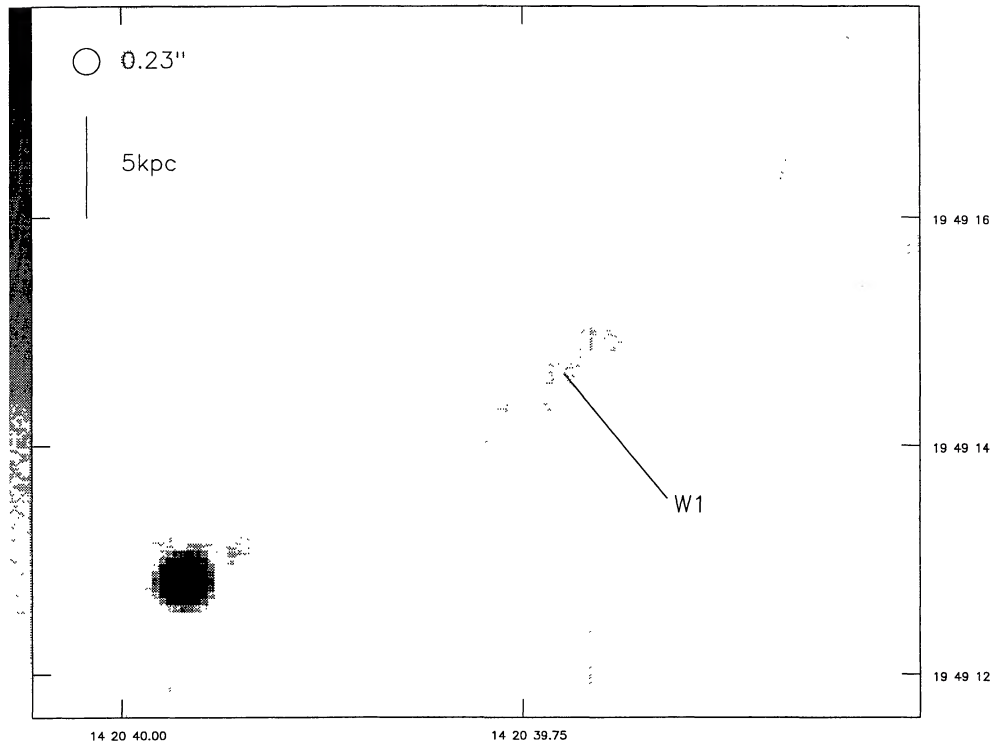


Figure 27. Core and jet of 3C 300 at 0.23-arcsec resolution. Linear grey-scale: black is $0.5 \text{ mJy beam}^{-1}$.

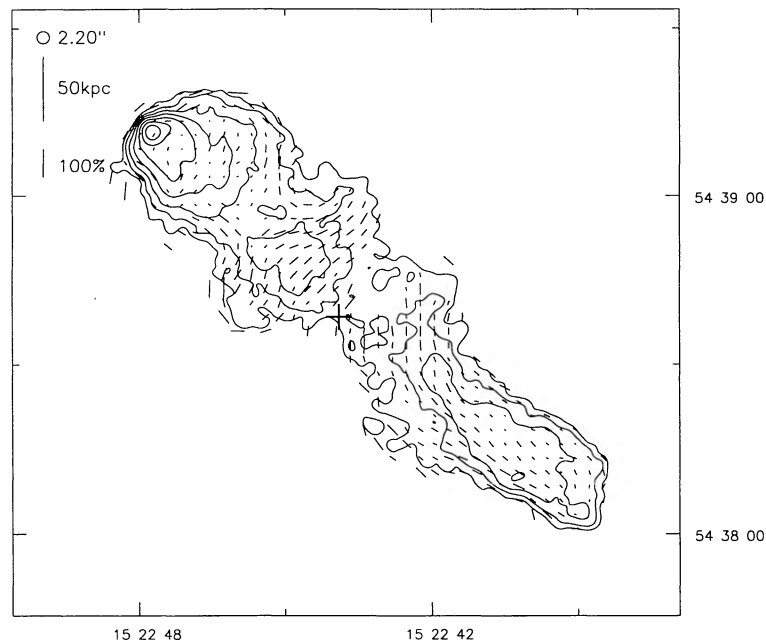


Figure 28. 3C 319 at 2.20-arcsec resolution. Contours at $0.2 \times (-2, -1, 1, 2, 4, \dots) \text{ mJy beam}^{-1}$. A cross marks the position of the optical identification.

field along its length turning to a transverse configuration as the jet enters the lobe, while the southern jet appears to have a magnetic field roughly transverse to its length (initially nearly north–south) as soon as polarization is detected. However, it is unsafe to infer magnetic field direction from the vectors shown here, as the depolarization at low frequencies may well indicate large differences in rotation measure across the source.

The high-resolution map (Fig. 39) shows the jets in detail. Both are unresolved or at best slightly resolved, and the opening angle is at most a few degrees. The northern jet (N1) is straight and, although it disappears before the end of the source, the structure there is consistent with the jet's terminating without bending further; the elongated knot at the far end of the lobe (N2) could be described as the beam termination hotspot, although it is not

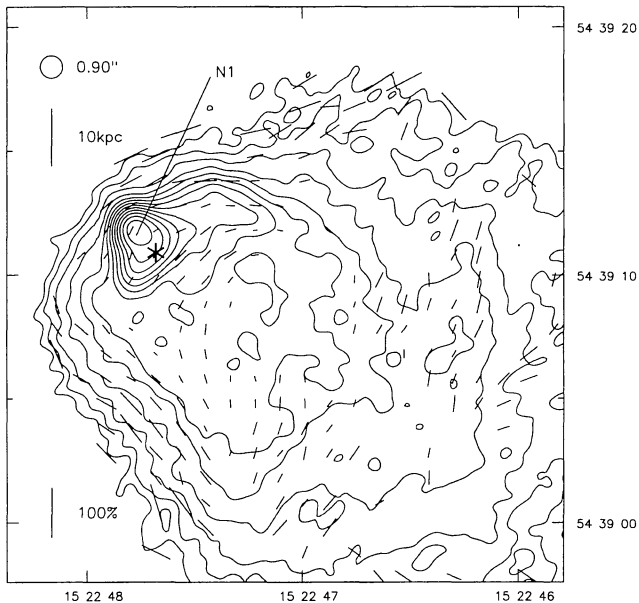


Figure 29. 3C 319 at 0.90-arcsec resolution. Contours at $1 \times (-\sqrt{2}, -1, 1, \sqrt{2}, 2, 2\sqrt{2}, \dots)$ mJy beam $^{-1}$. The position of the 20th magnitude object coincident with the hotspot is marked with an asterisk.

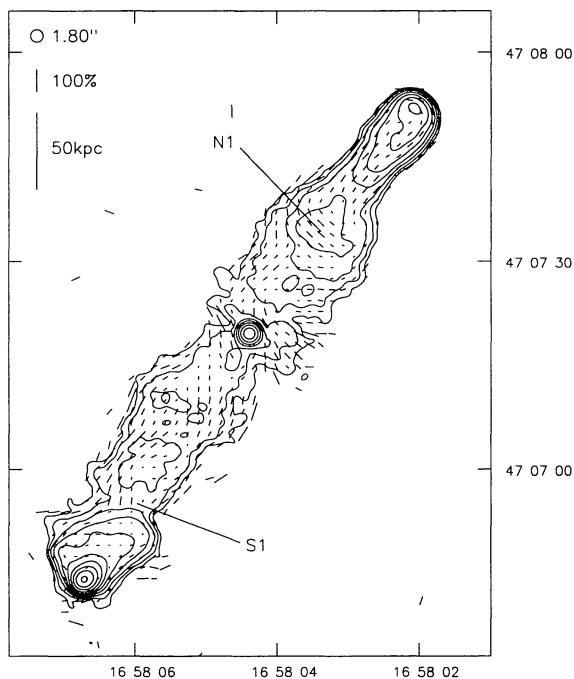


Figure 30. 3C 349 at 1.80-arcsec resolution. Contours at $0.25 \times (-2, -1, 1, 2, 4, \dots)$ mJy beam $^{-1}$.

separate from the bright structure to its north and east. The jet in the southern lobe (S1), on the other hand, is bent in several places: in fact, the jets do not make an angle of 180° at the core, so the beam must bend even before the jet becomes visible if they are initially oppositely directed. It can be traced to a bright knot in the middle of the lobe but its eventual termination point is not clear; it may be the bright region S2. The structures in the lobe – there are at least two separate hotspot regions – together with the bends in the jet are suggestive of a ‘flapping’ jet which may quite recently have been terminating in the southern end of the lobe. Both jets fade

significantly as they enter the bright parts of the lobes, and the tails of the lobes are curved at lower resolutions and frequencies (LP). These facts make a model plausible in which buoyancy due to the hot cluster gas has pushed the lobes away from the central regions of the source, leaving the jets to interact directly with the intergalactic medium (IGM) over most of their length (cf. Williams 1991). 3C 438 may thus have something in common with the class of WATs.

5 DISCUSSION

17 sources have been mapped in detail, with a resolution approaching 1 kpc in most cases. Quantitative analysis of the properties of the objects in this sample will be carried out in later papers; however, a few qualitative points about the images presented are made here.

5.1 Overall source properties

Four of the sources presented here (3C 123, 3C 171, 3C 401 and 3C 438) are not typical classical doubles. The first two have distorted lobes, but (as argued above) are probably nevertheless classical doubles in their essential physics; the last two have bright jets and diffuse hotspots. The jet of 3C 401 is one-sided; it may be related to the class of objects with dominant one-sided jets which have been given the name ‘jetted doubles’ by Law-Green et al. (1995). There are several similar objects with bright one-sided jets in the sample of B92 (e.g. 3C 15, 3C 277.3). 3C 438 appears unique in having bright dissipative twin jets which remain ‘FR II-like’ in their structure and opening angle, but may be related to the jetted-double class; if these are one-sided because of relativistic beaming, 3C 438 may be an example close to the plane of the sky, while if they are one-sided because of unusual dissipation on one side only, it seems plausible that there should exist two-sided versions. (The properties of this class of objects will be discussed in more detail in later papers.) The remaining sources in the sample, with the possible exception of 3C 319, are more or less conventional classical doubles.

The different shapes of the heads of the lobes have been pointed out in the text. As in the study of B92, there are many sources whose two lobes are very different from one another. Some of these differences may be attributed to short-time-scale variations of the beam termination behaviour (examples might include 3C 381 or 3C 349). In other cases (e.g. 3C 300) the differences must have been maintained over a long time-period, and if the beams themselves are symmetrical a strong environmental asymmetry is required. Particularly noticeable in this sample are the sources in which the hotspots are connected to the rest of the lobe by a long narrow ‘bottle-neck’, a feature also noticed by LP in their overlapping sample. Lobes of this kind, of which 3C 234 E is the prototype, are consistent with the working surface having encountered a sudden drop in the density of the external medium. The shape of the head of the lobe in simple models without variations in jet direction is governed by the relative velocities of hotspot advance (controlled by ram-pressure balance) plus backflow, and post-hotspot expansion, in which the material that has passed through the jet termination shock expands sideways into the shocked IGM as well as linearly into the cocoon. If the external density drops, ram-pressure balance ensures that the hotspot advance speed increases. The speed of sideways expansion should also increase, but, because the density of post-hotspot material should fall as the hotspot advance speed increases, the dependence of this speed on the external

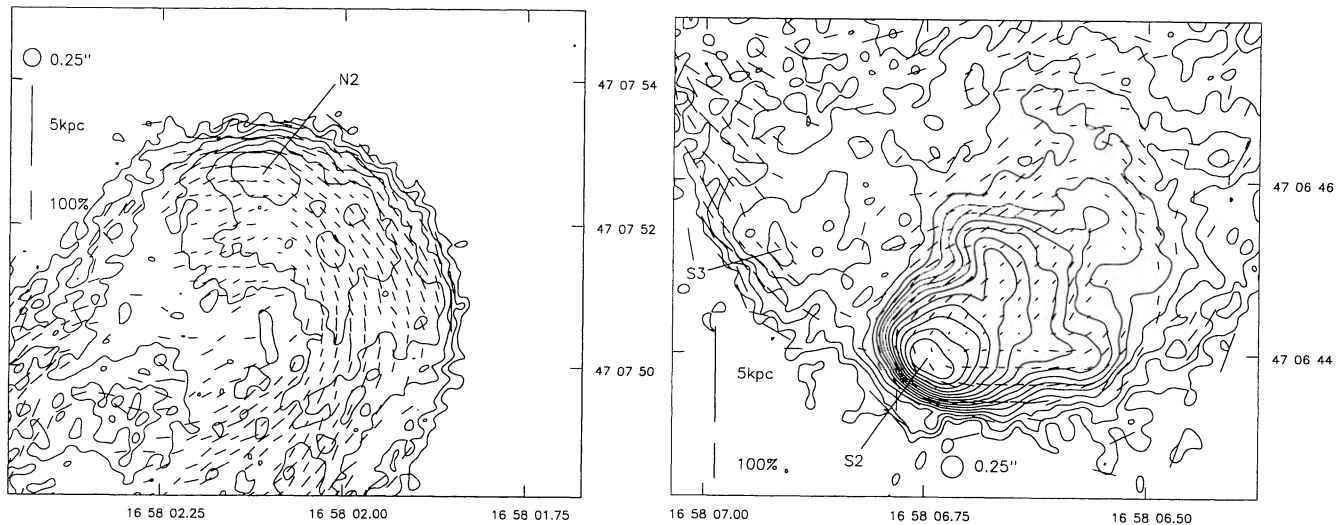


Figure 31. 3C 349 at 0.25-arcsec resolution. Left: northern hotspot; contours at $0.1 \times (-\sqrt{2}, -1, 1, \sqrt{2}, 2, 2\sqrt{2}, \dots)$ mJy beam $^{-1}$. Right: southern hotspot; contours as left.

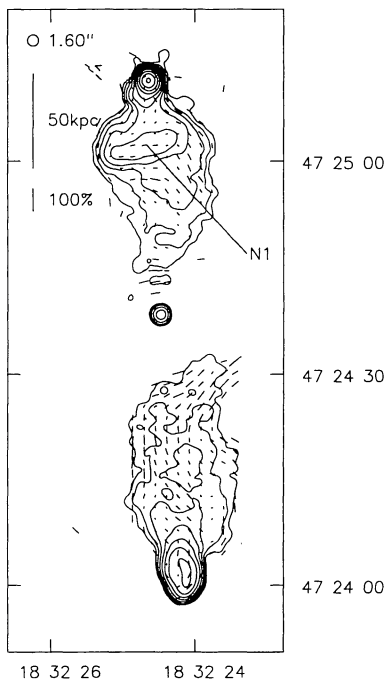


Figure 32. 3C 381 at 1.60-arcsec resolution. Contours at $0.4 \times (-2, -1, 1, 2, 4, \dots)$ mJy beam $^{-1}$.

density is weaker; the net effect is thus a narrowing of the head of the lobe. Sources such as 3C 234, where the bottle-neck is on scales comparable to the size of the whole source, are the exception rather than the rule, which suggests that in general variations in the jet direction can smooth out the front of the lobe. (3C 381 S may be an example of a lobe where this process is just about to occur.)

5.2 Hotspots

With the definition of hotspots that we have adopted, almost all sources in this sample have distinguishable hotspots in both lobes. L97 tabulate the positions and multiplicities of the hotspots in the low-redshift sample, and for comparison we have done the same, attempting to use comparable classifications. Table 6 summarizes

these properties. Hot spots are classed as single (1), double (2) or multiple (M); in addition, components 10 times fainter than the peak brightness of the hotspot complex are counted after a plus sign, so that '2+1' means 'double with an additional faint component'. Their location, as in L97, may be 'tip' (at the very end of the lobe), 'side' (on the lobe boundary, but not at the end) or 'middle' (anywhere else in the lobe). The location is of the whole hotspot complex, but we have noted cases where the location of the primary is significantly different. Comments are generally self-explanatory: 'diffuse' implies that there is little compact structure at the resolution of the map used, while 'extended' implies that a bright hotspot is significantly extended and so has a good chance of being resolved into multiple components at higher resolution. 'Rim' implies that multiple hotspots form a bright rim around the leading edge of the source or other structure in the hotspot complex; these features are common in the $z < 0.15$ sample (L97).

Double and multiple hotspots are common in this sample, as they were in that discussed by L97. Of the 42 lobes in Table 6, at least 18 (43 per cent) have more than one bright hotspot, which should be compared with ~ 50 per cent in the sample of L97. In the majority of such sources, one hotspot (the primary) is unambiguously more compact than any of the others, as in L89; these usually have a magnetic field direction transverse to the seen or inferred incoming beam direction. In the majority of these the primary hotspot is recessed with respect to the other components (although there are several counter-examples: 3C 79 E, 3C 234 E). The data presented here provide little direct evidence to identify the primary hotspot with the jet termination point; however, in two cases a jet is clearly seen to enter the primary hotspot (3C 234, 3C 436), and there are no cases in which a jet enters a secondary hotspot. These results are consistent with earlier work (L89). Most of the hotspots lie at the tip of the source; this trend is more pronounced than it was in L97, and there are fewer sources that show a distinct internal hotspot region (the clearest exception being 4C 14.11).

The physical significance of the numbers of hotspots is not clear. Higher-resolution observations of these objects would almost certainly reveal more hotspots (according to our classification) in a number of cases (compare the MERLIN and VLA images of 3C 123). The fundamental limit on the size-scale of emission from

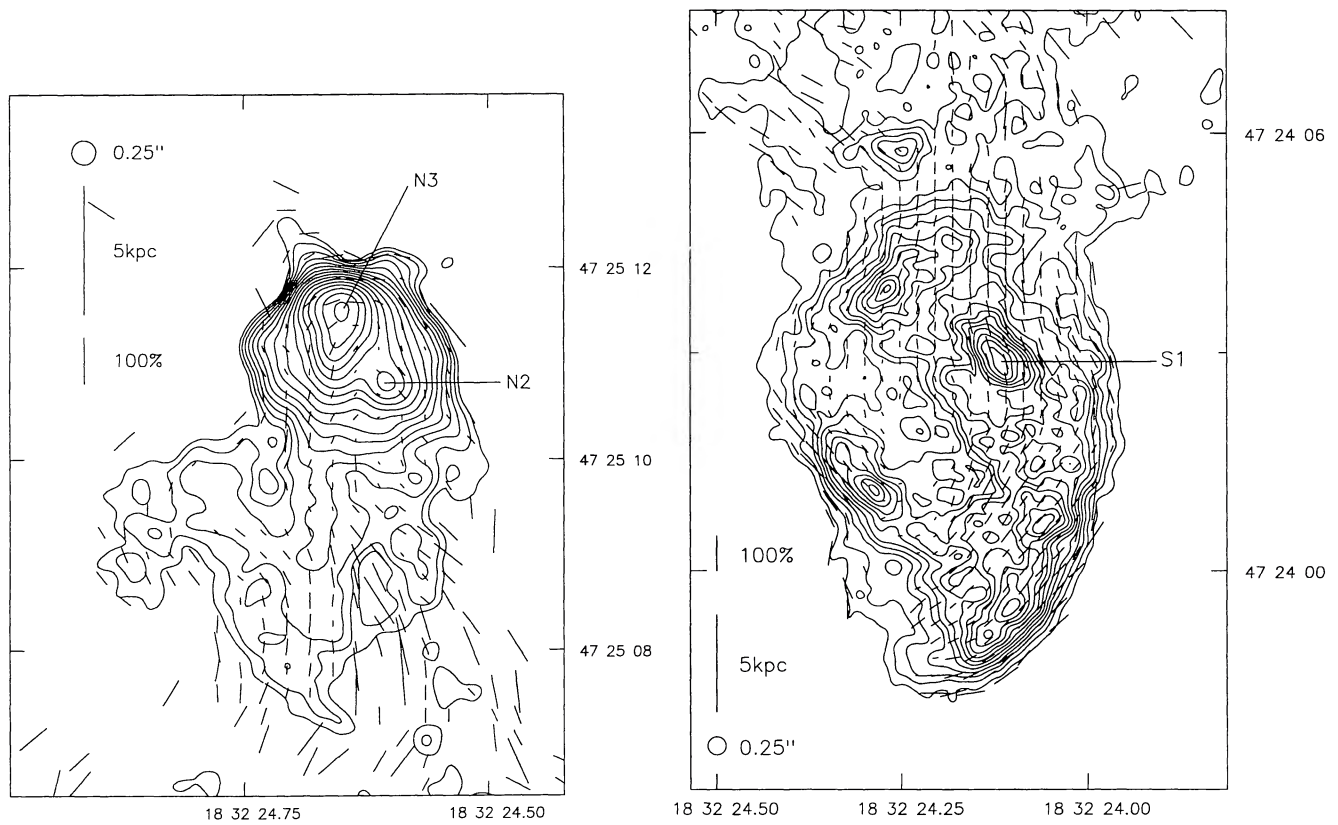


Figure 33. 3C 381 at 0.25-arcsec resolution. Left: northern hotspot; contours at $0.2 \times (-\sqrt{2}, -1, 1, \sqrt{2}, 2, 2\sqrt{2}, \dots)$ mJy beam $^{-1}$. Right: southern hotspot; as left but *linear* contours at $0.1 \times (-2, -1, 1, 2, 3, \dots)$ mJy beam $^{-1}$.

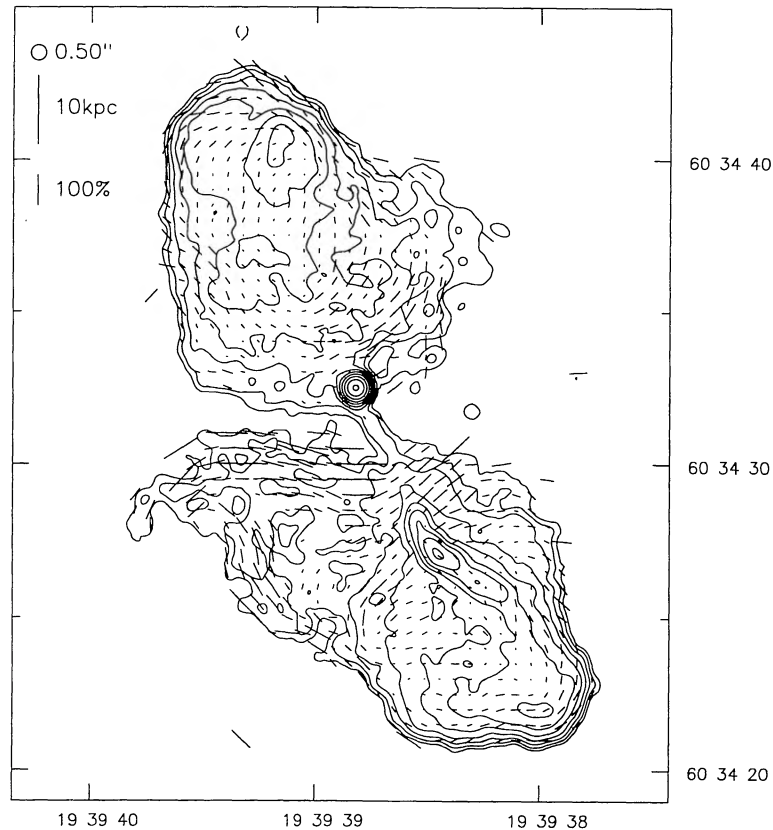


Figure 34. 3C 401 at 0.50-arcsec resolution. Contours at $0.1 \times (-2, -1, 1, 2, 4, \dots)$ mJy beam $^{-1}$.

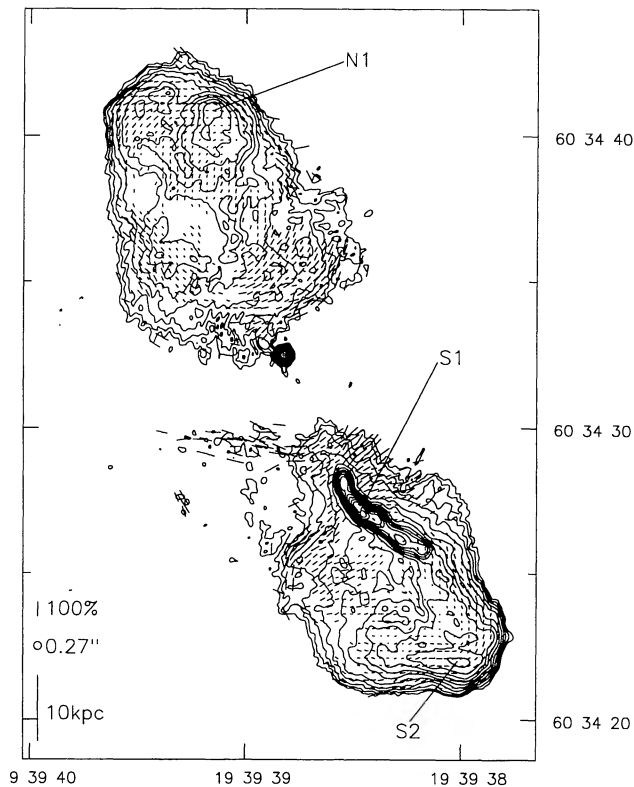


Figure 35. 3C 401 at 0.27-arcsec resolution. Contours at $0.1 \times (-\sqrt{2}, -1, 1, \sqrt{2}, 2, 2\sqrt{2}, \dots)$ mJy beam $^{-1}$.

the beam termination region is the cross-sectional size of the beam itself, and there is no reason to suppose that the spatial resolution achieved in this or other studies approaches that size. (The jet and hotspot in the southern lobe of 3C 436 provide some evidence that the jet width is not necessarily a good indicator of the beam width.) It is therefore hard to compare these results with those from other samples in an unbiased way. When we note that the hotspots in this sample seem less complicated than those of B92 and more complicated than those of L89, it must be borne in mind that this is certainly at least partly an effect of decreasing spatial resolution. Nevertheless, with this caveat, the overall impression is of a set of hotspots which, while being equally diverse, are slightly easier to classify and to understand in terms of pre-existing models than are those of B92 and L97.

The more diffuse (secondary) hotspots often have a magnetic field transverse to a line between themselves and the more compact hotspots. Although it is dangerous to argue too strongly from this, because this is often also the (circumferential) direction of the field lines in the rest of the end of the lobe, we have suggested in several particular cases that this, together with the bridges of emission linking the hotspots in several cases, implies that they are being fed directly from the compact hotspot [in a manner similar to that seen in the ‘splatter-spot’ models of Williams & Gull (1985) or the wall-jet mechanism of Norman & Balsara (1993); see also Laing (1982) and Lonsdale & Barthel (1986)] rather than being disconnected from the energy supply (as in the ‘dentist’s drill’ model of Scheuer 1982) or being fed by the remains of a discontinued beam (as in the models of Cox et al. 1991). In these last two models the magnetic field in secondary hotspots might be expected to remain transverse to the beam direction until the hotspot has expanded to be considerably

larger than the new primary; there are several compact secondaries in which this is certainly not the case. Equally, there are objects (e.g. 3C 123) that seem better fitted by the model of Cox et al. As the most recent numerical simulations can reproduce both types of secondary hotspot, the conclusion that there is no single model for multiple hotspots is probably uncontroversial. We believe, however, that the observations presented here provide further evidence for the possibility of comparatively well-collimated outflow from hotspots.

5.3 Jets

New jets are detected in 3C 20, 4C 14.11, 3C 234 and 3C 436; jets are confirmed and well imaged for the first time in a number of other sources (see Table 6). Jets that meet the criteria of Bridle & Perley (1984) unambiguously are found in 11 out of 21 objects, or 52 per cent. Possible jets are found in a further five objects [3C 132, 3C 153 and 3C 349 are discussed in the text; the possible jets in 4C 12.03 are discussed by LP and that in 3C 61.1 by Alexander (1985); we have also identified a knot in 3C 219 N as a possible counterjet]. The total number of jets detected may therefore be as high as 16, or 76 per cent. Only two objects have definite two-sided jets (3C 171, 3C 438), and both of these are unusual in other ways; there are possible two-sided jets in 3C 219, 3C 153, 4C 12.03 and (very tentatively) 3C 20, so that the number with two-sided jets may be six, or 29 per cent. With the exceptions of the jets in the unusual sources 3C 171, 3C 401 and 3C 438, and of those in the well-known objects 3C 219 and 3C 33.1, jets are generally faint, representing a very small fraction of the total flux of the source even at this high frequency, and can seldom be traced all the way from core to hotspot. These results are similar to those of Black (1992, 1993) and L97; the similar rate of jet detection allows us to conclude that the high rate of jet detection in that sample was not simply an effect of its proximity in luminosity to the FR I/FR II boundary.

The properties of the jets in the combination of the sample described here and that of B92, and their consequences for quasar–radio galaxy unification, will be discussed in a later paper.

ACKNOWLEDGMENTS

MJH acknowledges a research studentship from the UK Particle Physics and Astronomy Research Council (PPARC), and thanks the Astrophysics Group at the University of Bristol for support in the final stages of this paper’s preparation. We are grateful to Paddy Leahy, Katherine Blundell and Bill Cotton for allowing us to use VLA data obtained for other purposes, to Tom Muxlow for help with MERLIN data reduction, to Sigrid de Koff for permission to use the *HST* image of 3C 171, and to Robert Laing for supplying 5-GHz VLA data on 3C 123 and for providing information on the spectra of some of our sources in advance of publication. We thank the referee, Dr Rawlings, for his helpful comments. The National Radio Astronomy Observatory is operated by Associated Universities Inc., under cooperative agreement with the National Science Foundation. MERLIN is operated by the University of Manchester on behalf of PPARC. This project made use of Starlink facilities. This research has made use of the NASA/IPAC Extragalactic Database (NED) which is operated by the Jet Propulsion Laboratory, California Institute of Technology, under contract with the National Aeronautics and Space Administration.

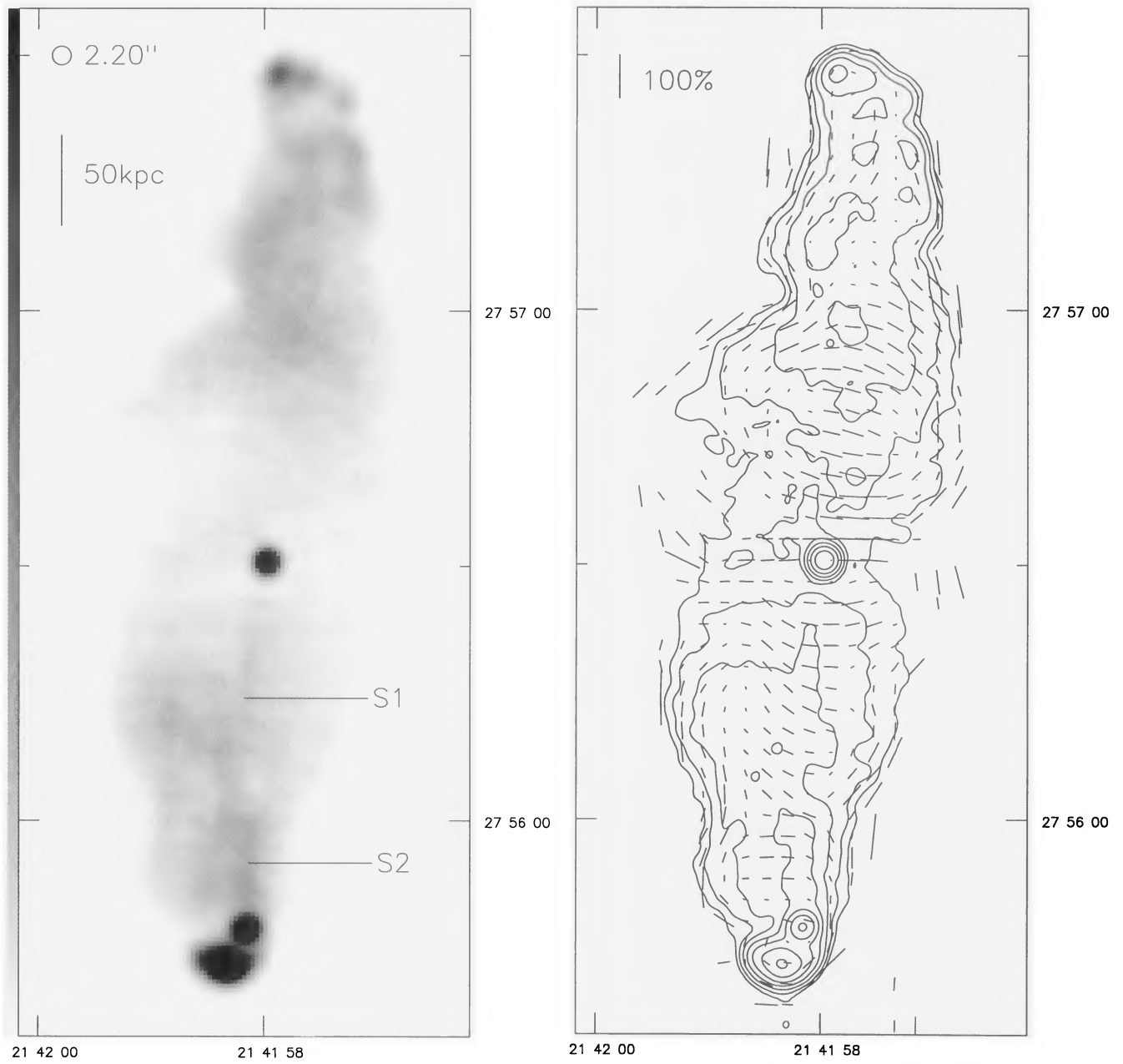


Figure 36. 3C 436 at 2.20-arcsec resolution. Left: linear grey-scale; black is 8 mJy beam^{-1} . Right: contours at $0.3 \times (-2, -1, 1, 2, 4, \dots) \text{ mJy beam}^{-1}$.

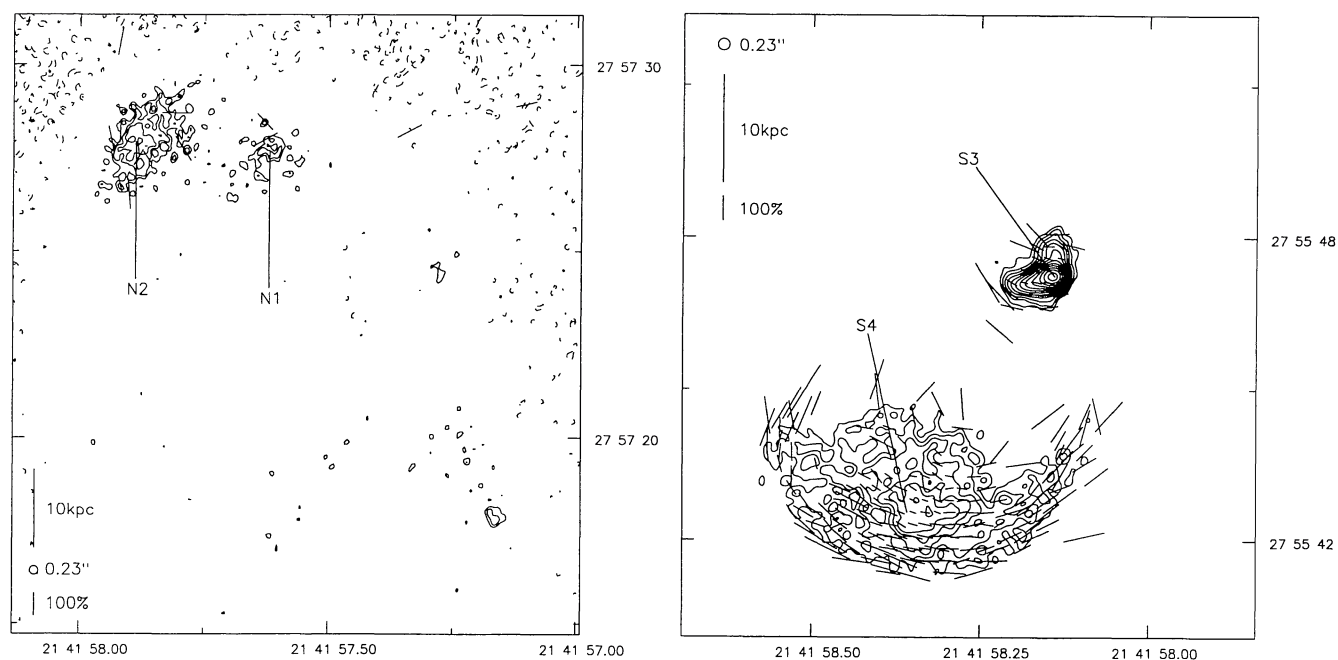


Figure 37. 3C 436 at 0.23-arcsec resolution. Left: northern hotspot; contours at $50 \times (-\sqrt{2}, -1, 1, \sqrt{2}, 2, 2\sqrt{2}, \dots) \mu\text{Jy beam}^{-1}$. Right: southern hotspot; as left but contours start at $100 \mu\text{Jy beam}^{-1}$.

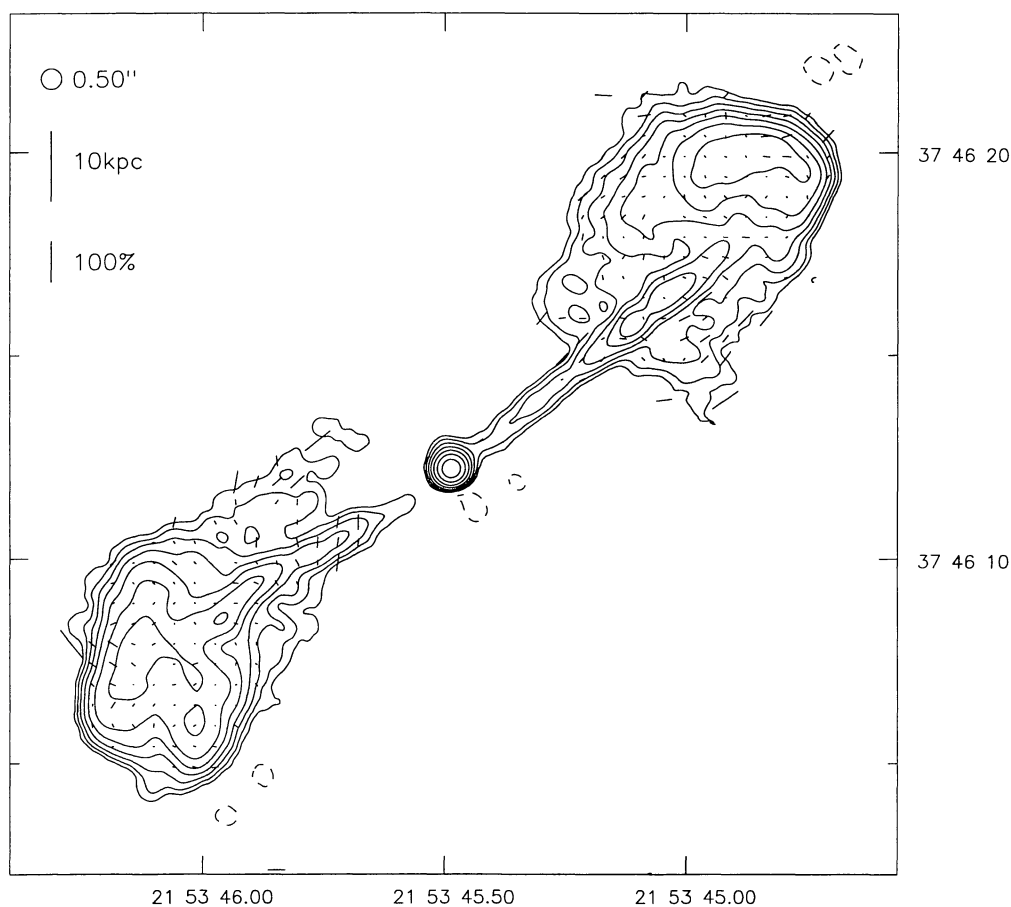


Figure 38. 3C 438 at 0.50-arcsec resolution. Contours at $0.15 \times (-2, -1, 1, 2, 4, \dots) \text{mJy beam}^{-1}$.

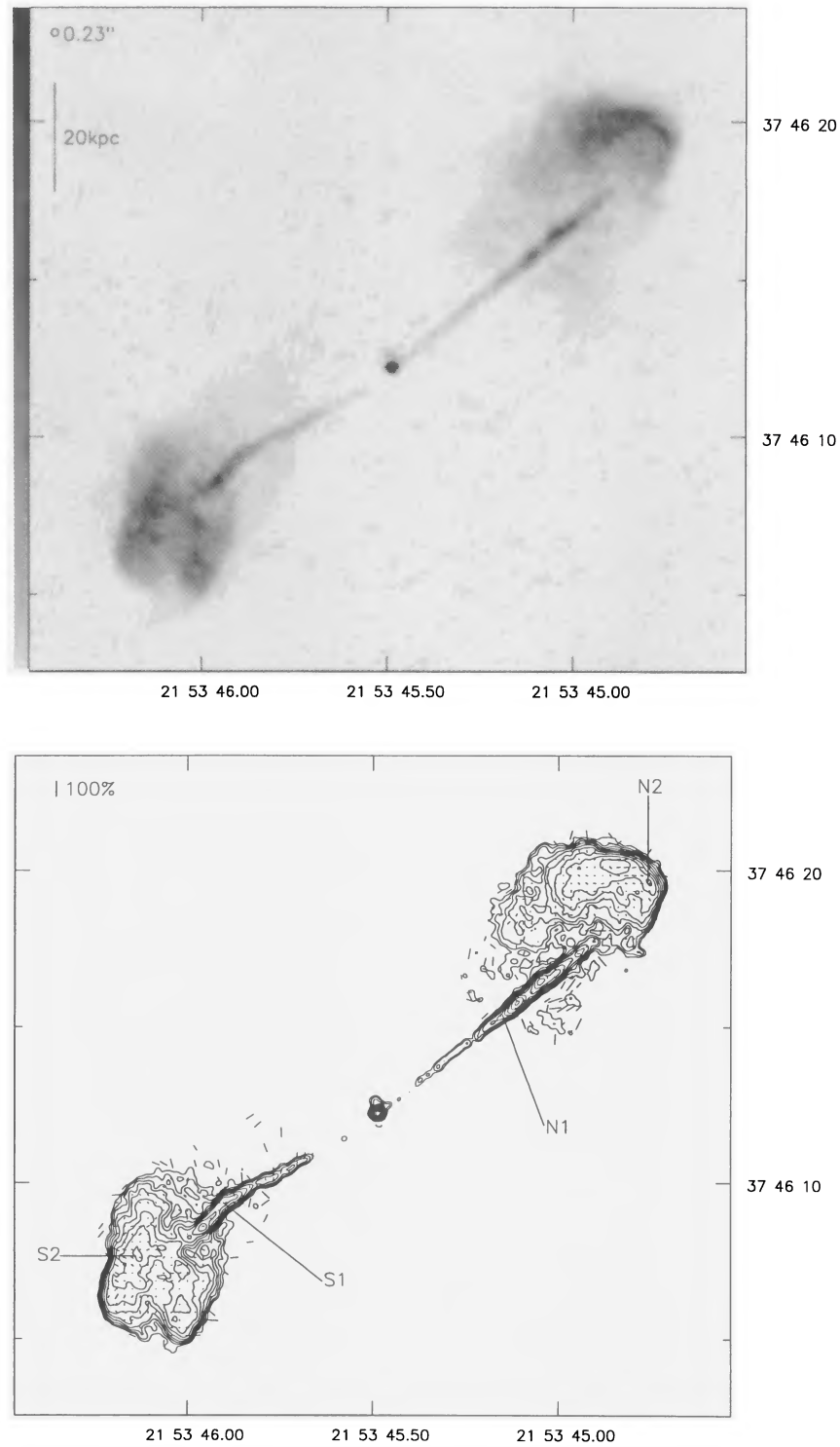


Figure 39. 3C 438 at 0.23-arcsec resolution. Above: linear grey-scale; black is 5 mJy beam^{-1} . Below: contours at $0.2 \times (-\sqrt{2}, -1, 1, \sqrt{2}, 2, 2\sqrt{2}, \dots) \text{ mJy beam}^{-1}$.

Table 6. Hotspots and jets.

Lobe	Type	Location	Comment	Jet?
4C 12.03 N	1	tip	diffuse	Y?
4C 12.03 S	1	tip		Y?
3C 20 E	2+1	tip	primary at side	Y?
3C 20 W	1+1	tip	tail	Y
3C 33.1E	1?	tip	low resolution	
3C 33.1W	1?	tip	low resolution	Y
3C 61.1 N	1	tip	extended	Y?
3C 61.1 S	1+1	tip	extended; recessed secondary	
3C 79 E	M+1	tip	rim?; recessed secondary	
3C 79 W	M	tip	rim	
4C 14.11 E	2+2	middle	secondary on edge	Y
4C 14.11 W	2	tip		
3C 123 E	2+M	tip	primary recessed; cylindrical; substructure	
3C 123 W	2	tip		
3C 132 E	2	tip	dim recessed secondary	Y?
3C 132 W	1	tip	tail	
3C 153 E	2	tip		Y?
3C 153 W	1	middle		Y?
3C 171 E	1	tip	jet enters hotspot	Y
3C 171 W	1	tip	jet enters hotspot	Y
3C 173.1 N	M	tip	rim	Y
3C 173.1 S	1	tip?	primary recessed, multiple sub-components	
3C 219 N	2	middle	curved rim around primary	Y?
3C 219 S	1	middle		Y
3C 234 E	1+2	tip	jet enters primary	Y
3C 234 W	2	tip	tails; rim?	
3C 284 E	2	tip		
3C 284 W	1	tip	extended	
3C 300 N	1?	tip	jet/hotspot confused	Y
3C 300 S	2+1	side	equal size	
3C 319 N	1	tip		
3C 319 S	0			
3C 349 N	1	tip	diffuse; tail?	
3C 349 S	1+1	tip	extended	
3C 381 N	1	tip	double substructure; primary recessed	
3C 381 S	M	tip		
3C 401 N	1	middle	diffuse	
3C 401 S	1	tip	jet enters; diffuse	Y
3C 436 N	M	tip	rim; diffuse	
3C 436 S	2	tip	jet enters recessed primary	Y
3C 438 E	1?	tip	jet nears; diffuse	Y
3C 438 W	2?	side	jet nears; diffuse	Y

REFERENCES

- Akujor C. E., Spencer R. E., Zhiang F. J., Davis R. J., Browne I. W. A., Fanti C., 1991, MNRAS, 250, 215
- Alexander P., 1985, PhD thesis, Univ. Cambridge
- Alexander P., 1987, MNRAS, 225, 27
- Alexander P., Leahy J. P., 1987, MNRAS, 224, 1
- Antonucci R. R. J., 1982, Nat, 299, 65
- Antonucci R., 1993, ARA&A, 31, 473
- Baars J. W. M., Genzel R., Pauliny-Toth I. I. K., Witzel A., 1977, A&A, 61, 99
- Black A. R. S., 1992, PhD thesis, Univ. Cambridge
- Black A. R. S., 1993, in Röser H.-J., Meisenheimer K., eds, Jets in Extragalactic Radio Sources. Springer-Verlag, Berlin, p. 15
- Black A. R. S., Baum S. A., Leahy J. P., Perley R. A., Riley J. M., Scheuer P. A. G., 1992, MNRAS, 256, 186 (B92)
- Blundell K. M., 1994, PhD thesis, Univ. Cambridge
- Blundell K. M., 1996, MNRAS, 283, 538
- Bridle A. H., Fomalont E. B., 1979, AJ, 84, 1679
- Bridle A. H., Perley R. A., 1984, ARA&A, 22, 319
- Bridle A. H., Fomalont E. B., Byrd G. G., Valtonen M. J., 1989, AJ, 97, 674
- Bridle A. H., Hough D. H., Lonsdale C. J., Burns J. O., Laing R. A., 1994, AJ, 108, 766
- Burch S. F., 1979, MNRAS, 186, 519
- Burns J. O., 1985, Can. J. Phys., 64, 373
- Burns J. O., Basart J. P., de Young D. S., Ghiglia D. C., 1984, ApJ, 283, 515
- Carilli C. L., Dreher J. W., Perley R. A., 1989, in Meisenheimer K., Röser H.-J., eds, Hotspots in Extragalactic Radio Sources. Springer-Verlag, Berlin, p. 51
- Clarke D. A., Bridle A. H., Burns J. O., Perley R. A., Norman M. L., 1992, ApJ, 385, 173
- Cox C. I., Gull S. F., Scheuer P. A. G., 1991, MNRAS, 252, 558
- Crane P., Tyson J. A., Saslaw W. C., 1983, ApJ, 265, 681
- de Koff S., Baum S. A., Sparks W. B., Biretta J., Golombek D., Machetto F., McCarthy P., Miley G. K., 1996, ApJS, 107, 621
- Dreher J. W., 1981, AJ, 86, 833

- Eales S. A., 1985a, MNRAS, 213, 899
 Eales S. A., 1985b, PhD thesis, Univ. Cambridge
 Eracleous M., Halpern J. P., 1994, ApJS, 90, 1
 Fanaroff B. L., Riley J. M., 1974, MNRAS, 167, 31P (FR)
 Feigelson E. G., Berg C. J., 1983, ApJ, 269, 400
 Feretti L., Gioia I. M., Giovannini G., Gregorini L., Padrielli L., 1984, A&A, 139, 50
 Giovannini G., Feretti L., Gregorini L., Parma P., 1988, A&A, 199, 73
 Grandi S. C., Osterbrock D. E., 1978, ApJ, 220, 783
 Hardee P. E., Norman M. L., 1990, ApJ, 365, 134
 Heckman T. M., van Breugel W. J. M., Miley G. K., 1984, ApJ, 286, 509
 Hiltner P. R., Meisenheimer K., Röser H. J., Laing R. A., Perley R. A., 1994, A&A, 286, 25
 Hughes P. A., Miller L., 1991, in Hughes P. A., ed., *Beams and Jets in Astrophysics*. Cambridge Univ. Press, Cambridge, p. 1
 Hutchings J. B., 1987, ApJ, 320, 122
 Hutchings J. B., Johnson I., Pyke R., 1988, ApJS, 66, 361
 Inoue M., Tabara H., Kato T., Aizu K., 1995, PASJ, 47, 725
 Jenkins C. J., Pooley G. G., Riley J. M., 1977, Mem. R. Astron. Soc., 84, 61 (JPR)
 Keel W. C., Martini P., 1995, AJ, 109, 2305
 Laing R. A., 1981, MNRAS, 195, 261
 Laing R. A., 1982, in Heeschen D. S., Wade C. M., eds, *Proc. IAU Symp. 97, Extragalactic Radio Sources*. Reidel, Dordrecht, p. 161
 Laing R., 1989, in Meisenheimer K., Röser H.-J., eds, *Hot Spots in Extragalactic Radio Sources*. Springer-Verlag, Berlin, p. 27 (L89)
 Laing R. A., Riley J. M., Longair M. S., 1983, MNRAS, 204, 151 (LRL)
 Laing R. A., Jenkins C. R., Wall J. V., Unger S. W., 1994, in Bicknell G. V., Dopita M. A., Quinn P. J., eds, *ASP Conf. Ser. Vol. 54, The First Stromlo Symposium: The Physics of Active Galaxies*. Astron. Soc. Pac., San Francisco, p. 201
 Law-Green J. D. B., Leahy J. P., Alexander P., Allington-Smith J. R., van Breugel W. J. M., Eales S. A., Rawlings S. G., Spinrad H., 1995, MNRAS, 274, 939
 Lawrence C. R., Pearson T. J., Readhead A. C. S., Unwin S. C., 1986, AJ, 91, 494
 Leahy J. P., Perley R. A., 1991, AJ, 102, 537 (LP)
 Leahy J. P., Williams A. G., 1984, MNRAS, 210, 929
 Leahy J. P., Pooley G. G., Riley J. M., 1986, MNRAS, 222, 753
 Leahy J. P., Black A. R. S., Dennett-Thorpe J., Hardcastle M. J., Komissarov S., Perley R. A., Riley J. M., Scheuer P. A. G., 1997, MNRAS, in press (L97)
 Longair M. S., Gunn J. E., 1975, MNRAS, 170, 121
 Lonsdale C. J., Barthel P. D., 1986, AJ, 92, 12
 Lonsdale C. J., Morison I., 1983, MNRAS, 203, 833
 McCarthy P. J., Spinrad H., van Breugel W., 1995, ApJS, 99, 27
 Macklin S. T., 1983, MNRAS, 203, 147
 Meisenheimer K., Röser H.-J., Hiltner P. R., Yates M. G., Longair M. S., Chini R., Perley R. A., 1989, A&A, 219, 63
 Muxlow T. W. B., Garrington S. T., 1991, in Hughes P. A., ed., *Beams and Jets in Astrophysics*. Cambridge Univ. Press, Cambridge, p. 52
 Myers S. T., Spangler S. R., 1985, ApJ, 291, 52
 Neff S. G., Roberts L., Hutchings J. B., 1995, ApJ, 99, 349
 Norman M. L., Balsara D. S., 1993, in Röser H.-J., Meisenheimer K., eds, *Jets in Extragalactic Radio Sources*. Springer-Verlag, Berlin, p. 229
 Perley R. A., 1989, in Meisenheimer K., Röser H.-J., eds, *Hot Spots in Extragalactic Radio Sources*. Springer-Verlag, Berlin, p. 1
 Perley R. A., Carilli C. L., 1996, in Carilli C. L., Harris D. E., eds, *Cygnus A – Study of a Radio Galaxy*. Cambridge Univ. Press, Cambridge, p. 168
 Rawlings S., 1987, PhD thesis, Univ. Cambridge
 Rawlings S., Saunders R., Eales S. A., Mackay C. D., 1989, MNRAS, 240, 701
 Riley J. M., Pooley G. G., 1975, Mem. R. Astron. Soc., 80, 105
 Riley J. M., Pooley G. G., 1978, MNRAS, 183, 245
 Riley J. M., Longair M. S., Gunn J. E., 1980, MNRAS, 192, 233
 Rudnick L., 1984, in Bridle A. H., Eilek J. A., eds, *Physics of Energy Transport in Radio Galaxies*, Proc. NRAO Workshop No. 9. NRAO, Green Bank, p. 35
 Sandage A. R., 1973, ApJ, 180, 687
 Scheuer P. A. G., 1982, in Heeschen D. S., Wade C. M., eds, *Proc. IAU Symp. 97, Extragalactic Radio Sources*. Reidel, Dordrecht, p. 163
 Simard-Normandin M., Kronberg P. P., Button S., 1981, ApJS, 45, 97
 Smith H. E., Spinrad H., Smith E. O., 1976, PASP, 88, 621
 Spangler S. R., Myers S. T., Pogge J. J., 1984, AJ, 89, 1478
 Spencer R. E. et al., 1991, MNRAS, 250, 225
 Spinrad H., 1978, ApJ, 220, L135
 Spinrad H., Djorgovski S., Marr J., Aguilar L., 1985, PASP, 97, 932
 Stephens P., 1987, PhD thesis, Univ. Manchester
 Taylor G. L., Dunlop J. S., Hughes D. H., Robson E. I., 1996, MNRAS, 283, 930
 Williams A. G., 1991, in Hughes P. A., ed., *Beams and Jets in Astrophysics*. Cambridge Univ. Press, Cambridge, p. 342
 Williams A. G., Gull S. F., 1985, Nat, 313, 34
 Wyndham J. D., 1966, ApJ, 144, 459
 Zukowski E., 1990, PhD thesis, Univ. Toronto

This paper has been typeset from a $\text{T}_{\text{E}}\text{X}/\text{L}^{\text{A}}\text{T}_{\text{E}}\text{X}$ file prepared by the author.